Nekhoroshev's approach to Hamiltonian monodromy

Dmitriĭ A. Sadovskiĭ *
Département de physique, Université du Littoral – Côte d'Opale, 59140 Dunkerque, France

August 16, 2016

Abstract

On the example of the hyperbolic circular billiard, introduced in [Europhys. Lett. **83**, 24003 (2008)] by Delos *et al* as, possibly, the most simple system with Hamiltonian monodromy, we illustrate the method developed by N. N. Nekhoroshev and co-authors [Ann. H. Poincaré **7**(6), 1099–1211 (2006)] to uncover this phenomenon. Nekhoroshev's very original geometric approach reflects his profound regard at Hamiltonian monodromy as a general topological property of fibrations. We take advantage of the possibility to have closed form elementary function expressions for all quantities in our system in order to provide most explicit and detailed explanation of Hamiltonian monodromy and its relation to similar phenomena in other domains.

Mathematics Subject Classification (2000): 34C20 37J35 53D20 55R55

Keywords: integrable fibration, Hamiltonian monodromy, first homology, A_1 singularity

file: nnmethod TEXed 2016-11-07 07:48

1 Introduction

The term *monodromy* appears in several domains of mathematics. Typically, it describes what happens after we go once ($\mu o \nu o$) around a closed path ($\delta \rho o \mu o \sigma$). Monodromy relates global and local structures. The two well known examples, both originating in the first third of the 20th century, are the Picard–Lefschetz monodromy in complex geometry and monodromy of the Poincaré map near a stable periodic orbit.

Hamiltonian monodromy, as the most basic topological obstruction to the existence of *global* action-angle coordinates in Hamiltonian dynamical systems, was introduced in mechanics by Duistermaat [33], who returned the earlier idea of Nekhoroshev [50, 51, 52] about extending local action-angle coordinates whose existence is guaranteed, under certain sufficiently general assumptions, by the Liouville–Arnold theorem[1] [6, 11]. Several examples of concrete fundamental mechanical systems with nontrivial monodromy followed [28, 20, 15, 25]. During the same period, we witness extensive

*Electronic mail: sadovski@univ-littoral.fr

[1] As is often the case, several other names may be associated with this theorem: Nekhoroshev [52] suggests Poincaré and Lyapunov, while Vũ Ngọc and Nguyên Tiên point to a similar statement by Mineur [47].

progress by Arnol'd and co-workers in the theory of singularities [8–10, 12] where Picard–Lefschetz monodromy becomes the basic component. So mechanics and complex geometry develop in parallel.

Most generally, we encounter monodromy in the geometry of fibre bundles. To characterize a bundle we begin with describing the topology of the full space, the base space, the regular fibres Λ (which have the same topology) and various critical fibres Λ_*. The base space is naturally stratified into the sets of images of Λ and Λ_*. The image of all critical fibres in the base forms a *bifurcation diagram*, connected components of the image of the regular fibres constitute *lower cells*. Moving along paths in the base space corresponds to deforming fibres and to their bifurcations [16]. Monodromy appears in this context when we attempt to describe how fibres "fit together" in the full space of the bundle. To this end we study *connections*, i.e., continuous bijective maps between regular fibres Λ, in conjunction with the topology of the base. We ask whether the bundle (Λ, R) of regular fibres Λ over a lower cell R is trivial, i.e., whether it is isomorphic to $\Lambda \times \mathsf{R}$. When the topology of R is nontrivial, the answer is typically negative. Monodromy appears when the fundamental group $\pi_1(\mathsf{R})$ is nontrivial, i.e., when there are closed loops $\gamma \subset \mathsf{R}$ which are not homotopic to 0.

In this paper, we consider monodromy in a system of a particle moving in a circular billiard with axially-symmetric negative quadratic potential, one of the simplest Hamiltonian systems with monodromy proposed by Delos et al. [31, 32]. Because all computations for this system can be made explicitly in terms of elementary functions[2], this example is particularly suited for scrutinizing Hamiltonian monodromy and its relation to similar phenomena in other domains. So we demonstrate the equivalence of monodromy in our system (and thus in any Hamiltonian system with a nondegenerate focus-focus equilibrium) to the Picard-Lefschetz monodromy associated with the A_1 singularity. Our main purpose, however, is to explain the global section method which was introduced by Nekhoroshev and co-workers [48, 49, 53] in order to understand, at first, the "usual" or "integer" monodromy on the example of the $1{:}(-1)$ resonance, and subsequently compute the "fractional" monodromy of the $1{:}(-2)$ resonance. We will see that through his approach Nekhoroshev gives the most direct relation of Hamiltonian monodromy to the topology of integrable fibrations.

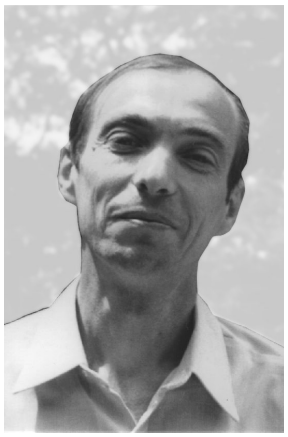

Nikolaí N. Nekhoroshev
1946–2008

N. N. Nekhoroshev [1] became interested in the problem of global action-angle variables in the very early years of his mathematical research activity. In his first scientific publication [50], which was based on the results of his MSc diploma work at the Moscow State University, he studied action-angle variables in superintegrable systems. He continued this work in [51, 52]. Already at that time he had realized that the most basic obstacle to global action-angle variables was nontrivial monodromy. However, systems with monodromy were seen as abstract formal mathematical examples, very distant from real dynamical systems. Numerous concrete, often fundamental physical systems with monodromy were uncovered much later following Duistermaat [33] and Cushman [28]. Nekhoroshev learned of the physical importance of monodromy after meeting Zhilinskií in 2001 and began his long-term collaboration with Zhilinskií and Sadovskií, physicists working at the Université du Littoral in Dunkerque, France. As a result of his involvement, Nekhoroshev made a spectacular comeback to this

[2] We like to note that all illustrations in this paper are computed, none is just hand-drawn.

field by introducing generalized or fractional Hamiltonian monodromy [48, 49], a clearcut new concept which, at the time, had no predecessor in the theory of Hamiltonian dynamical systems, and which still has to find analogs in complex analysis and singularity theory. His keen interest in the subject (see [53, 54]) continued up until his sudden severe illness in May 2008, one week before his new scheduled visit to Dunkerque. His many new ideas [55] that he was so eager to discuss with his colleagues physicists had never come to light.

The outline of the paper is as follows. The definition of monodromy (sec. 3) uses the first homology H_1 of the regular fibres Λ of the integrable fibration. We should describe also the base of the fibration and its singular fibres. All this requires concrete information on the system which we gather in sec. 2. In sec. 2.4, we also explain the equivalence of our fibration and the one in the case of the A_1 singularity. Using these concrete results, we construct basis cycles for $H_1(\Lambda)$ and compute monodromy in sec. 3. We do this in parallel for our Hamiltonian system and for the equivalent A_1 singularity (Picard-Lefschetz monodromy). The latter is considered for the sake of comparison with the Nekhoroshev-style computation (proof) of Hamiltonian monodromy which is presented in sec. 4. We observe further in sec. 5 that Nekhoroshev treats Hamiltonian monodromy very generally, reaching across different domains of mathematics and remaining close to the spirit of the Picard-Lefschetz theory. So, among various methods to compute Hamiltonian monodromy, his can be seen by right as related directly to "geometric monodromy theorems".

2 Analysis of the classical mechanical system

We describe analytically our system. Particular applications in subsequent sections rely on parts of this description. In sec. 2.2 and 2.7, we pay substantial attention to the $\mathrm{SO}(2)$ symmetry. As Nekhoroshev himself used to point out, this symmetry analysis is not imperative to understanding monodromy. So some readers may safely skip it. On the other hand, most of our analytical and geometrical description can be obtained more elegantly and understood more fully if the $\mathrm{SO}(2)$ symmetry of the system is exploited. More importantly, a normal form argument shows that such symmetry is locally inherent in a neighbourhood of *any* focus-focus (or complex hyperbolic) equilibrium [56, 57, 69, 55].

2.1 Hyperbolic circular billiard

Consider a linear Hamiltonian dynamical system with two degrees of freedom which is defined on the phase space $\mathrm{T}^*\mathbb{R}^2 \sim \mathbb{R}^4$ with canonical coordinates $\mathbf{q} = (x,y)$ and $\mathbf{p} = (p_x, p_y)$ and standard symplectic form $\omega = \mathrm{d}x \wedge \mathrm{d}p_x + \mathrm{d}y \wedge \mathrm{d}p_y$, and which is described by the simple Hamiltonian[3]

$$H(x,y,p_x,p_y) = \frac{1}{2\mu}(p_x^2 + p_y^2) - \frac{a}{2}V(x,y) \tag{2.1a}$$

with $a > 0$, $\mu > 0$, where $V(x,y)$ is an axially symmetric potential function

$$V(x,y) = \begin{cases} x^2 + y^2 = \rho^2, & \rho \le \rho_{\max}, \\ -\infty, & \rho > \rho_{\max}. \end{cases} \tag{2.1b}$$

[3] Delos et al. [32] call H "unperturbed" Hamiltonian and denote as H_0, while its value h is denoted E

Rescaling the system with Hamiltonian (2.1a), we can set without loss of generality[4]

$$\mu = a = 1, \tag{2.1c}$$

and retain one single parameter $\rho_{\max}$. We can think of a particle of mass $\mu > 0$ moving in a circular billiard with hard wall of radius $\rho_{\max}$ and scattering quadratic potential of height $\rho_{\max}^2/2$. Potential (2.1b) restricts all configurations $\mathbf{q}$ to a closed disk $\bar{B} = \{\|\mathbf{q}\| \leq \rho_{\max}\} \subset \mathbb{R}^2$ and our phase space is, in fact, the subspace $\mathrm{T}^*\bar{B} = \{(\mathbf{q},\mathbf{p}) \in \mathrm{T}^*\mathbb{R}^2, \mathbf{q} \in \bar{B}\}$. Without the wall, i.e., in the limit $\rho_{\max} = \infty$, we obtain a simple scattering system with the phase space $\mathrm{T}^*\mathbb{R}^2$. For simplicity, we call $\mathbb{R}^4$ the phase space even when $\rho_{\max}$ is finite.

2.2 Axial $\mathrm{SO}(2)$ symmetry and discrete symmetries

The system $(H, \mathrm{T}^*\mathbb{R}^2, \omega)$ with H in (2.1) is invariant under symplectic $\mathbb{S}^1$ action

$$\mathbb{S}^1 \times \mathrm{T}^*\mathbb{R}^2 \to \mathrm{T}^*\mathbb{R}^2 : (t, (\mathbf{q},\mathbf{p})) \mapsto (S^t\mathbf{q}, S^t\mathbf{p}) = \mathrm{diag}(S^t, S^t)\,\mathbf{u} \tag{2.2a}$$

with 2×2 orthogonal matrix

$$S^t = \begin{pmatrix} \cos t & -\sin t \\ \sin t & \cos t \end{pmatrix}. \tag{2.2b}$$

These simultaneous rotations in the $\mathbf{q}$ and $\mathbf{p}$ planes about their origins constitute the Lie symmetry group $\mathrm{SO}(2)$ of the system, also called *axial* symmetry. We can also see that reflections σ of either symplectic 2-plane in any line passing through 0, for example

$$\sigma : (\mathbf{q},\mathbf{p}) \mapsto (S_\sigma\mathbf{q}, S_\sigma\mathbf{p}) \quad \text{with} \quad S_\sigma = \mathrm{diag}(-1,1), \tag{2.3}$$

are also symplectic and leave $(H, \mathrm{T}^*\mathbb{R}^2, \omega)$ unchanged. Combined with $\mathrm{SO}(2)$, operations (2.3) constitute the full phase space symmetry group $\mathrm{SO}(2) \wedge \sigma = \mathrm{O}(2) = D_\infty$ (in the Schönflies notation) of the system. Operations S^t and $S_\sigma S^t$ form conjugacy classes $\mathbf{1}$, $S^{\pm t}$ with $t \in (0,\pi)$, S^π, and σ (all improper rotations) of this group.

Remark 2.1 (orbits of $\mathrm{SO}(2) \wedge \sigma$). The $\mathrm{SO}(2)$ action (2.2) on $\mathrm{T}^*\mathbb{R}^2 \sim \mathbb{R}^4$ is *not free*. Its generic orbits are circles defined in by (2.2) with $\mathbf{u} \neq \mathbf{0}$, while the origin $\mathbf{u} = \mathbf{0} \in \mathbb{R}^4$ is a *fixed point* of the action which forms an isolated critical one-point orbit. The $\mathrm{O}(2)$ action has the same orbits.

Existence of the critical orbit $\mathbf{0}$ has immediate consequences: any $\mathrm{O}(2)$ invariant Morse-Bott function on $\mathrm{T}^*\mathbb{R}^2$, such as H, has an isolated critical point $\mathbf{0}$, and the respective Hamiltonian system has an equilibrium at 0. The consequences for the reduction of the $\mathrm{O}(2)$ symmetry are discussed in sec. 2.7.

In addition to symplectic symmetries (2.2) and (2.3), Hamiltonian (2.1) remains invariant under the reversal symmetry

$$\mathcal{T} : (\mathbf{q},\mathbf{p}) \mapsto (\mathbf{q}, -\mathbf{p}), \tag{2.4}$$

often called *time reversal*[5] in physics. $\mathcal{T}$ commutes with σ. So the full spatio-temporal symmetry group of H is $\mathrm{O}(2) \times \mathcal{T}$. Taking (2.4) into account may simplify the analysis.

[4] In some of the formulae, symbolic coefficients μ and a are kept to facilitate dimensionality checks

[5] $\mathcal{T}$ has the same effect on the trajectories of the system as reversing time in the equations of motion; a more exact terminology, however, is *momentum reversal*

2.2.1 Polar coordinates

Traditionally, physicists account for symmetry (2.2) by introducing polar canonical coordinates $(\rho,\phi,p_\rho,p_\phi)$, where $\rho\geq 0$ is the radius in the (x,y) plane,

$$\phi := \varphi_q = \tan^{-1}(y/x), \tag{2.5}$$

is the polar angle, and (p_ρ,p_ϕ) are momenta conjugate to (ρ,ϕ). In such coordinates, Hamiltonian (2.1a) becomes function of $(\rho,,p_\rho,p_\phi)$ only, with p_ϕ conserved. The disadvantage of $(\rho,\phi,p_\rho,p_\phi)$ is their own singularity at $\rho=0$ which obscures correct geometry, cf. [36]. We parallel certain aspects of our description in terms of $(\rho,\phi,p_\rho,p_\phi)$, see, e.g., sec. 2.7.5.

2.2.2 Basic invariants

Instead of polar coordinates (ρ,p_ρ,p_ϕ) the dynamics of the system can be described in terms of *invariants* of the $\mathrm{O}(2)$ group action in (2.2) and (2.3) which are smooth everywhere on $\mathrm{T}^*\mathbb{R}^2$ and which are straightforwardly constructed as polynomials in $(\mathbf{q},\mathbf{p})$ using invariant theory. We provide some detail to illustrate the practical aspects and applications in normal forms and Euler-Poisson reduction.

Lemma 2.2. *The Molien generating function characterizing the ring of all polynomials in* $\mathbf{u}=(\mathbf{q},\mathbf{p})=(x,y,p_x,p_y)$ *invariant under the* $\mathrm{SO}(2)$ *action* (2.2a) *is*

$$g(\lambda) = (1+\lambda^2)/(1-\lambda^2)^3 \tag{2.6a}$$

with Hilbert form

$$g(\lambda) = (1-\lambda^4)/(1-\lambda^2)^4. \tag{2.6b}$$

Proof. The construction is most simple in rotated coordinates $\xi=\frac{1}{2}(x+\mathrm{i}y)$ and $\eta=\frac{1}{2}(p_x+\mathrm{i}p_y)$ which diagonalize (2.2) and transform as

$$\big(t,(\xi,\eta,\bar\xi,\bar\eta)\big)\mapsto U^t(\xi,\eta,\bar\xi,\bar\eta),\quad \text{with } U^t=\mathrm{diag}(\mathrm{e}^{\mathrm{i}t},\mathrm{e}^{-\mathrm{i}t},\mathrm{e}^{\mathrm{i}t},\mathrm{e}^{-\mathrm{i}t}).$$

The function (2.6a) can be computed directly from the Molien theorem by integrating over the $\mathbb{S}^1$ group [72]

$$g(\lambda)=\frac{1}{2\pi}\int_0^{2\pi}\frac{dt}{\det(1-\lambda U^t)}=\frac{1}{2\pi\mathrm{i}}\oint_{|s|=1}\frac{s\,ds}{(1-\lambda s)^2(s-\lambda)^2}, \tag{2.7a}$$

where λ is a formal real variable representing any of $(\xi,\eta,\bar\xi,\bar\eta)$, and where we used the explicit form of U^t and complex unimodular variable $s=\mathrm{e}^{\mathrm{i}t}$ to obtain the standard Cauchy integral on the right-hand side. Since λ is used to Taylor expand $g(\lambda)$ at 0, its value can be assumed arbitrarily small. So for $|\lambda^{-1}|>1$, our integral has a single pole $s=\lambda$ of order 2 within the unit circle $|s|=1$, and the Cauchy integral formula

$$g(\lambda)=\frac{\partial}{\partial s}\frac{s}{(1-\lambda s)^2}\bigg|_{s=\lambda} \tag{2.7b}$$

yields the Molien function (2.6a) in the lemma. The Hilbert form (2.6b) is obtained by multiplying both numerator and denominator of (2.6a) on $(1-\lambda^2)$. □

The ring of all SO(2)-invariant polynomials in $(\xi,\eta,\bar\xi,\bar\eta)$ is generated by four linearly independent quadratic invariants represented by the denominator terms of (2.6b). They are related by one quartic algebraic relation or *sygyzy* of the first order represented by the numerator term. We can choose four invariants $\theta_1=\xi\bar\xi$, $\theta_2=\eta\bar\eta$, $\theta_3=\xi\bar\eta$, and $\theta_4=\eta\bar\xi$ obeying the relation[6] $\theta_1\theta_2=\theta_3\theta_4$. To a factor, the first two invariants equal the radius square

$$R=\tfrac12(x^2+y^2)=\tfrac12\,\mathbf{q}^2=\tfrac12\rho^2\ge 0 \tag{2.8a}$$

and the kinetic energy

$$T=\tfrac12(p_x^2+p_y^2)=\tfrac12\,\mathbf{p}^2=\tfrac12(p_\rho^2+m^2\rho^{-2})\ge 0, \tag{2.8b}$$

respectively. Alternatively, we can use rotated invariants

$$X=\tfrac12(T+R)\ge 0 \quad\text{and}\quad Y=\tfrac12(T-R). \tag{2.9}$$

Replacing the remaining θ_3 and θ_4 for real polynomials

$$J_1=2\mathrm{i}\,(\theta_3-\theta_4)=xp_y-yp_x=\mathbf{q}\wedge\mathbf{p}=p_\phi, \tag{2.10a}$$
$$K=\theta_3+\theta_4=\tfrac12(xp_x+yp_y)=\tfrac12\,\mathbf{q}\cdot\mathbf{p}=\tfrac12\rho p_\rho, \tag{2.10b}$$

we can rewrite their relation as

$$TR=K^2+\tfrac14 J_1^2 \quad\text{or}\quad 2\Phi(X,Y,K):=X^2-Y^2-K^2=\tfrac14 J_1^2, \tag{2.11}$$

with obvious restrictions

$$0\le R\le R_{\max}=\tfrac12\rho_{\max}^2, \quad T\ge 0, \quad X\ge 0. \tag{2.12}$$

Because of (2.11), the ring of SO(2)-invariant polynomials is *not free*. The Molien function (2.6a) suggests that we can have three principal (denominator) quadratic generators and one auxiliary (numerator) generator, also quadratic. Then any polynomial in the ring can be expressed as a polynomial in the three principal generators times an at most linear polynomial in the auxiliary one. Specifically, we have

Lemma 2.3. *Choosing (X,Y,K) and J_1 as principal and auxiliary invariants, the ring of polynomials in $(\mathbf{q},\mathbf{p})$ invariant under the* SO(2) *action* (2.2) *can be represented as*

$$\mathcal{R}(X,Y,K)\bullet\{1,J_1\},$$

where $\mathcal{R}$ is a free module generated multiplicatively by (X,Y,K).

Such construction is known as polynomial *integrity basis* [46], homogeneous system of parameters [62], or Hironaka decomposition [63], and is generally possible for Cohen-Macauley rings [62]. The integrity or integral basis terminology goes back to Weyl [72], who, however, did not distinguish between principal and auxiliary generators and meant only using integer powers of all generators while supplying all algebraic relations between them, he named sygyzies. One can also use rational functions of integer powers of generators, a rational integrity basis, which was studied early in [18] and which is known to require lesser number of auxiliary invariants.

The system of invariants can be modified further by accounting for discrete symmetries σ and $\mathcal{T}$ in sec. 2.2. We come to

[6] this relation is quadratic in the invariants themselves but quartic in the variables $(\xi,\eta,\bar\xi,\bar\eta)$

Lemma 2.4. *All* $\mathrm{O}(2)$ *polynomial invariants form the free module* $\mathcal{R}(X,Y,K)$*; all* $\mathrm{O}(2)\wedge\mathcal{T}$ *invariants can be described as* $\mathcal{R}(X,Y,K^2)\subset\mathcal{R}(X,Y,K)$.

Proof. Consider the action of σ and $\mathcal{T}$ on $(\mathbf{q},\mathbf{p})$ and verify that

$$\sigma:(R,T,J_1,K)\mapsto(R,T,-J_1,K), \tag{2.13a}$$

$$\mathcal{T}:(R,T,J_1,K)\mapsto(R,T,-J_1,-K). \tag{2.13b}$$

In other words, R and T (and their linear combinations X and Y) are fully $\mathrm{O}(2)\times\mathcal{T}$ symmetric, K is $\mathrm{O}(2)$ symmetric, while J_1 changes sign under both σ and $\mathcal{T}$. Dropping the auxiliary invariant J_1 in lemma 2.3 (which is a covariant), we realize that the ring of $\mathrm{O}(2)$ invariants is generated freely by T, R, and K. Using K^2 instead of K, we select all $\mathrm{O}(2)\times\mathcal{T}$ invariants. □

Lemma 2.4 can be illustrated by appropriate transformations of (2.6a). The auxiliary invariant J_1 is $\mathrm{O}(2)$-covariant and we should exclude all polynomials containing J_1. To this end, we can simply omit the numerator term λ^2 that represents J_1 and obtain the Molien function

$$g_{\mathrm{O}(2)}(\lambda)=1/(1-\lambda^2)^3$$

for the $\mathrm{O}(2)$-invariant polynomials. To account also for the reversal symmetry $\mathcal{T}$, we replace the $\mathcal{T}$-covariant K by K^2. Transforming $g_{\mathrm{O}(2)}$ accordingly into

$$g_{\mathrm{O}(2)}(\lambda)=(1+\lambda^2)/\left((1-\lambda^4)(1-\lambda^2)^2\right)$$

and dropping λ^2 in the numerator which stands for K, we obtain

$$g_{\mathrm{O}(2)\times\mathcal{T}}(\lambda)=1/\left((1-\lambda^4)(1-\lambda^2)^2\right).$$

Remark 2.5. We can see from (2.11) that the basis (X,Y,J_1^2) also suits the purpose of expressing all $\mathrm{O}(2)\times\mathcal{T}$ invariants.

Remark 2.6. Expressing the $\mathcal{T}$-invariant Hamiltonian function (2.1) as

$$H=T-R=2Y, \tag{2.14}$$

we see the benefit of using (2.9) instead of (2.8). At the same time, the dynamics under H is not $\mathcal{T}$-invariant and the reduced equations of motion require using (X,Y,K), see sec. 2.7.6. So functions (X,K) replace the "traditional" (ρ,p_ρ).

Additional restrictions imposed by the hard wall In our system (2.1), for any given value m of J_1, the value h of H is bound from below:

$$h\geq h_{\min}(m)=\frac{m^2}{4R_{\max}}-R_{\max}. \tag{2.15}$$

The minimum energy $h_{\min}$ corresponds to the particle with $K=0$ and $R=R_{\max}$ remaining all the time at the wall and moving on the circular orbit along the wall if $m\neq 0$. Furthermore, for any given fixed (m,h) we obtain

$$X\leq X_{\max}=\tfrac{1}{2}h+R_{\max} \tag{2.16a}$$

and

$$|K|\leq K_{\max}(m,h)=\sqrt{R_{\max}\left(R_{\max}+h\right)-\tfrac{1}{4}m^2}=\tfrac{1}{2}\sqrt{(2X_{\max})^2-f^2}, \tag{2.16b}$$

where $X=X_{\max}$ and $K=\pm K_{\max}$ correspond to the particle reaching the wall. The lowest possible values $R_{\min}(m,h)$ and $X_{\min}(m,h)$ of R and X will be given later. Such values are attained away from the hard wall when $K=0$, see sec. 2.6.

2.3 First integrals: momentum J_1 and energy H. Energy-momentum map $\mathcal{EM}$, integrable fibration

In this section, we discuss those aspects of the geometry that are insensitive to the $\|\mathbf{q}\| \leq \rho_{\max}$ cutoff, whose the nontrivial consequences will be analyzed later, after considering hard wall reflections in sec. 2.5.

2.3.1 Integrability

The angular momentum J_1 in (2.10a) is the *momentum* of the SO(2) action (2.2). The 2π-periodic flow

$$\varphi^t_{J_1} : \mathbb{R} \times \mathrm{T}^*\mathbb{R}^2 \to \mathrm{T}^*\mathbb{R}^2 : (t, \mathbf{u}) \mapsto S^t_{J_1}\mathbf{u}, \quad \text{with} \quad S^t_{J_1} = \mathrm{diag}(S^t, S^t) \tag{2.17}$$

of its linear Hamiltonian vector field X_{J_1} defines the $\mathbb{S}^1$ orbits of (2.2). Notice that here and elsewhere $\mathbf{u} = (\mathbf{q}, \mathbf{p})^T$. By the Noether theorem, J_1 is the first integral of our SO(2) symmetric system. The latter is, therefore, integrable. We can verify this directly by computing that J_1 and H in (2.1) Poisson commute, $\{J_1, H\} = 0$. We can also show that the flow

$$\varphi^t_H : \mathbb{R} \times \mathrm{T}^*\mathbb{R}^2 \to \mathrm{T}^*\mathbb{R}^2 : (t, \mathbf{u}) \mapsto S^t_H\mathbf{u}, \tag{2.18a}$$

with

$$S^t_H = \begin{pmatrix} \cosh t & 0 & \sinh t & 0 \\ 0 & \cosh t & 0 & \sinh t \\ \sinh t & 0 & \cosh t & 0 \\ 0 & \sinh t & 0 & \cosh t \end{pmatrix}, \tag{2.18b}$$

of the Hamiltonian vector field X_H (for $\mathbf{q} < \rho_{\max}$) commutes with the flow $\varphi^t_{J_1}$ of X_{J_1}, that is $\varphi^t_{J_1} \circ \varphi^t_H = \varphi^t_H \circ \varphi^t_{J_1}$. This follows from the matrix commutation relation $S^t_{J_1} S^t_H = S^t_H S^t_{J_1}$. The flow (2.18) preserves the values m and h of momentum J_1 and energy H.

2.3.2 Integrable fibration

The integrable map

$$\mathcal{EM} = (J_1, H) : \mathrm{T}^*\mathbb{R}^2 \to \mathbb{R}^2 : \mathbf{u} = (\mathbf{q}, \mathbf{p})^T \mapsto (J_1(\mathbf{u}), H(\mathbf{u})) = (m, h) \tag{2.19}$$

given by the pair of Hamiltonian functions (J_1, H) in involution is called the *energy-momentum map*[7]; it is also known as generalized momentum map because J_1 is a momentum of an $\mathbb{S}^1$ action, while H is not. Points $(\mathbf{q}, \mathbf{p})$ at which the Jacobian $\partial(J_1, H)/\partial(\mathbf{q}, \mathbf{p})$ has rank smaller than the maximal value 2 and the corresponding values (m, h) are, respectively, *critical points* and *critical values* of $\mathcal{EM}$.

The map $\mathcal{EM}$ defines fibration of $\mathrm{T}^*\mathbb{R}^2$ whose fibres $\Lambda_{(m,h)} := \mathcal{EM}^{-1}(m, h)$ are combined constant (m, h)-level sets of (J_1, H). The base of this fibration is a closed half-plane (see fig. 1)

$$\bar{\mathsf{R}} = \{(m, h), h \geq h_{\min}(m)\} \subset \mathbb{R}^2 \tag{2.20a}$$

which is a closure of the set of regular $\mathcal{EM}$ values

$$\mathsf{R} = \{(m, h), h > h_{\min}(m)\} \setminus \{(0, 0)\}. \tag{2.20b}$$

[7] Contrary to what the sequence in the name "energy-momentum" may imply, the historical convention [21] is to use momentum m and energy h as the first (horizontal axis) and second (vertical axis) coordinate in $\mathbb{R}^2$. So the values of $\mathcal{EM}$ are denoted (m, h), respectively.

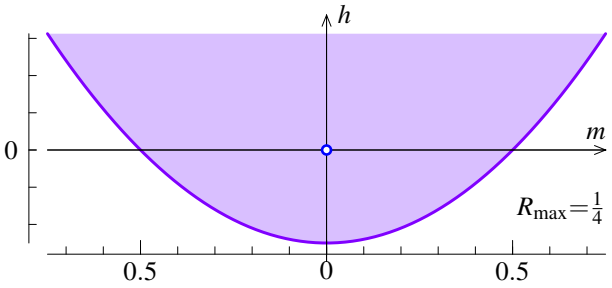

Figure 1: Image of the energy-momentum map $\mathcal{EM}$ (2.19) of the system with Hamiltonian (2.1) and $R_{\max} = 1/4$. Shaded area represents the set (2.20b) of regular $\mathcal{EM}$ values, solid lower boundary represents relative equilibria, the opaque circle marks the isolated critical value $(0,0)$.

Critical fibres correspond to $\mathcal{EM}$ values in $\partial\mathsf{R}$ and contain at least one critical point. Below, we characterize critical and regular values (m,h) and corresponding fibres.

Lemma 2.7 (fibres of $\mathcal{EM}$)**.** *All fibres $\Lambda_{(m,h)}$ of (2.19) are connected. Without cutoff $\mathbf{q} \le \rho_{\max}$, all regular fibres are diffeomorphic to a cylinder $\mathbb{R}\times\mathbb{S}^1$. Critical fibres include a continuous one-parameter family of* relative equilibria *$\Lambda_{(m,h_{\min}(m))}$ and the exceptional fibre $\Lambda_{(0,0)}$. The former are smooth circles $\mathbb{S}^1$. The fibre $\Lambda_{(0,0)}$ is a union of two right half-cones joint at their singular points which represent the unstable equilibrium $\mathbf{0}\in\mathrm{T}^*\mathbb{R}^2$. This fibre can be viewed as a cylinder pinched at one point. At all points of $\Lambda_{(m,h_{\min}(m))}$, the vector fields X_{J_1} and X_H are collinear and the rank of $\partial(J_1,H)/\partial(\mathbf{q},\mathbf{p})$ is 1. This rank equals 2 on $\Lambda_{(0,0)}\setminus\mathbf{0}$ and drops to 0 at the equilibrium $\mathbf{0}$. The cutoff $\mathbf{q}\le\rho_{\max}$ compactifies all fibres.*

The above statements can be proven using explicit proper immersions

$$\mathrm{emb}_v : \Lambda_{(m,h)} \hookrightarrow \mathbb{R}^3_{v,K} \quad \text{with } v = q,p$$

of $\Lambda_{(m,h)}$ in the space $\mathbb{R}^3$ with coordinates[8] (x,y,K) or (p_x,p_y,K) where $|K|\le K_{\max}(m,h)$, which we call q and p embeddings respectively, see fig. 2, top. For example, substituting $T = h+R$ in (2.11) we obtain the q-embedding

$$\mathrm{emb}_q\,\Lambda_{(m,h)} = \left\{(x,y,K),\ 4K^2+(m^2+h^2) = (x^2+y^2+h)^2\right\}.$$

The q-embedding is singular (and cannot be used) for $m=0$ and $h\ge 0$; the p-embedding is singular for $m=0$ and $h_{\min}<h\le 0$. For $m=h=0$, each embedding represents $\Lambda_{(0,0)}$ as a right cone.

In the special case of $K_{\max}(m,h)=0$, the fibre becomes a smooth circle $\mathbb{S}^1$, which is a relative equilibrium. From (2.16) we can see that this fibre exists for all m when h equals

$$h_{\min}(m) = m^2/(4R_{\max}) - R_{\max} = \tfrac{1}{2}\left(m^2\rho_{\max}^{-2} - \rho_{\max}^2\right). \tag{2.21}$$

We can also see from (2.16) that in general the energy equals $K_{\max}^2/R_{\max} + h_{\min}$, i.e., is superior to $h_{\min}$. □

Away from $\{m=0\}$, the images of $\Lambda_{(m,h)}$ under the two embeddings are diffeomorphic and can be used to define two different trivializations of the fibre as illustrated in

[8] In polar coordinates, one may attempt replacing K by p_ρ. Then *no* embedding will be useful for $m=0$.

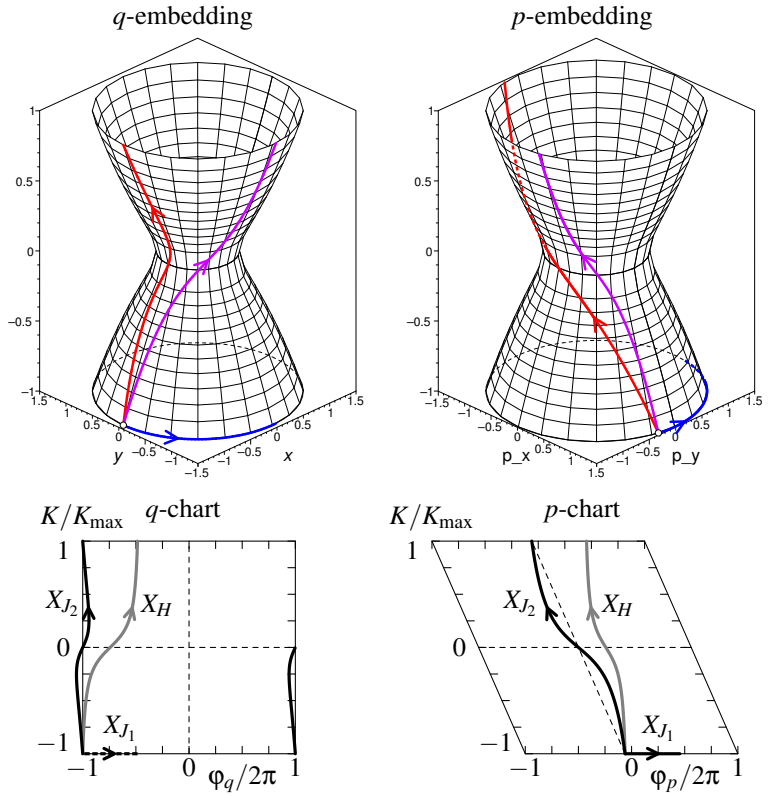

Figure 2: Representation of the trajectory of the system with Hamiltonian H in (2.1) (gray bold curve) on a regular fibre $\Lambda_{(m,h)}$ (with $m = 0.4$ and $h = 0.1$) using the q-embedding (left) and the p-embedding (right). Bold solid directed curves represent orbits of the flow of the Hamiltonian vector fields X_H, X_{J_2}, and X_{J_1} launched at the same point on $\Lambda_{(m,h)}$ and propagated forward in time for one period $\tau(m,h)$ of the first return. Dashed lines on the two-dimensional charts in the lower row connect (glue) identical points. Rotation angle $\theta(m,h)$ corresponds to the displacement along the orbit of X_{J_1}, i.e., along the $\mathbb{S}^1$ orbit of the $\mathrm{SO}(2)$ group action (2.2).

fig. 2, bottom row. The angle coordinates of these q and p trivializations are the polar angle φ_q and its dual angle

$$\varphi_p := \tan^{-1}(p_y/p_x), \tag{2.22}$$

in the $\mathbf{p}$-plane, respectively. For any given $m \neq 0$, the correspondence between the trivializations follows from

$$\tan(\varphi_p - \varphi_q) = \frac{\mathbf{q}\wedge\mathbf{p}}{\mathbf{q}\cdot\mathbf{p}} = \frac{J_1}{2K} = \frac{m}{2K}, \tag{2.23a}$$

and therefore

$$\varphi_p - \varphi_q = \frac{\pi}{2} - \tan^{-1}\frac{2K}{m}. \tag{2.23b}$$

So in particular, at the moment of the impact this gives

$$\varphi_p + \alpha = \varphi_q + \tfrac{1}{2}\pi \quad \text{with} \quad \alpha = \tan^{-1}\frac{2K_{\max}}{m}, \tag{2.24}$$

as will be also read directly off fig. 4(a) later.

Remark 2.8. Notice that when $R_{\max} \gg |h+\mathrm{i}m| = |f|$, the angle α has values in a small interval that shrinks to $\pi/2$ as $R_{\max} \to \infty$. This means that sufficiently far from $\mathbf{0}$, the motion becomes essentially one-dimensional: the particle moves almost along radial lines with $|p_\rho| \gg |p_\phi|$.

2.4 Relation to the A_1 singularity

Consider the bijective linear map

$$\Psi : \mathrm{T}^*\mathbb{R}^2 \to \mathbb{C}^2 : (x, y, p_x, p_y) \mapsto (u, w) = \frac{1}{\sqrt{2}}(\mathrm{i}x + p_y, \mathrm{i}y - p_x) \tag{2.25}$$

of the phase space $\mathrm{T}^*\mathbb{R}^2 \sim \mathbb{R}^4$ to the complex plane $\mathbb{C}^2$ with coordinates (u, w). From (2.1) and (2.10a) we can see that under (2.25)

$$H + \mathrm{i}J_1 = u^2 + w^2 =: F(u, w), \tag{2.26}$$

and we obtain the following diagram

$$\begin{array}{ccc} \mathbb{R}^4 & \xrightarrow{\Psi} & \mathbb{C}^2 \\ {\scriptstyle (J_1, H)}\downarrow & & \downarrow{\scriptstyle F} \\ \mathbb{R}^2 & \xrightarrow{\psi} & \mathbb{C} \end{array} \tag{2.27}$$

where the values f of the complex-valued function F in (2.26) are related to the values (m, h) of (J_1, H) by[9]

$$\psi : \mathbb{R}^2 \to \mathbb{C} : (m, h) \mapsto h + \mathrm{i}m = f. \tag{2.28}$$

This shows that the (m, h)-level set $\Lambda_{(m,h)} \subset \mathrm{T}^*\mathbb{R}^2$ of the energy-momentum map $\mathcal{EM}$ in (2.19) is diffeomorphic to the f-level set $\Lambda_f \subset \mathbb{C}^2$ of F in (2.26).

Observe also that under (2.25) the standard symplectic structure on $\mathrm{T}^*\mathbb{R}^2$ induces on $\mathbb{C}^2$ a Poisson structure

$$\{u, \bar{w}\} = \{\bar{u}, w\} = \{w, \bar{w}\} = \{\bar{u}, u\} = 0, \quad \{u, w\} = -\mathrm{i}. \tag{2.29}$$

Furthermore, using (2.29) we obtain

$$\{H, F\} = \{J_1, F\} = 0. \tag{2.30}$$

This makes dynamics of the real system (with $\|\mathbf{q}\| < \rho_{\max}$) and that of the complex system with Hamiltonian F equivalent.

The origin $0 \in \mathbb{C}$ is an isolated critical value of F. The corresponding fibre $\Lambda_0 = \{u = 0\} \cap \{w = 0\}$ is known as the A_1 *singularity*, and is the most basic type in the classification [12, 10, 9, 8]. Under the map (2.25) this fibre is, necessarily, diffeomorphic to the union $\Lambda_{(0,0)}$ of two half-cones described in the previous section. The typical representation of the regular f-level sets of (2.26) uses the Riemann surface S_f of

$$u \mapsto w = \sqrt{f - u^2} \tag{2.31}$$

[9] The standard orientation of $\mathbb{C}$ implied by this map differs from that we have in $\mathbb{R}^2$ due to our specific choice of axes, see sec. 2.3 and footnote 7.

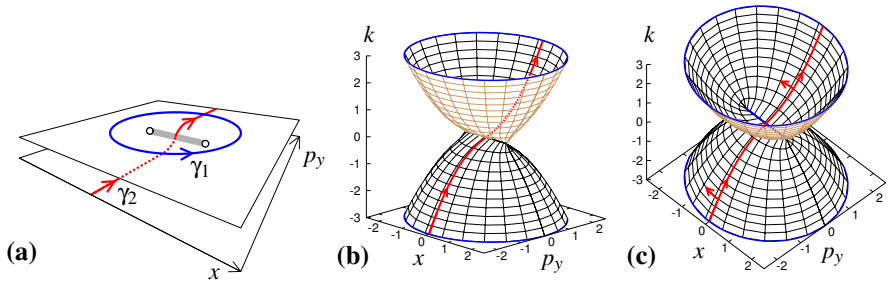

Figure 3: (a) Schematic representation of the Riemann surface S_f of (2.31) for $\mathrm{Re}\, f < 0$ and $\mathrm{Im}\, f = 0$; the two planes interleave along the bold gray line that connects the branch points at $\pm f^{1/2}$ indicated by opaque circles. (b) The same surface defined as regular fibre Λ_f of (2.26) immersed in $\mathbb{R}^3$ with coordinates (x, p_y, k). (c) Orientation of the surface in (b).

which is constructed of two copies of $\mathbb{C}^1$ with coordinate u glued together at two *branch points* $u = \pm\sqrt{f}$ and interleaved along the "cut" connecting the branch points. Thus, when $f \in \mathbb{R}_{<0}$, i.e., for $h < 0$ and $m = 0$, the branch points are $(x, p_y) = (\pm\sqrt{|f|}, 0)$ and the cut can be made along the interval $\{|x| < \sqrt{|f|}, p_y = 0\}$.

Hand-sketched illustrations (see for example the Introduction in [9, 10] and [12]) usually represent the two $\mathbb{C}^1$ as two $\mathbb{R}^2$ planes embedded in $\mathbb{R}^3$, see fig. 3(a). It can be seen that any path γ_1 that encircles the cut remains on the same plane, while any path γ_2 that crosses the cut, passes from one plane to another. Below we construct an *explicit embedding*

$$\mathrm{emb}_u : \Lambda_f \hookrightarrow \mathbb{C}_u \times \mathbb{R}_k = \mathbb{R}^3_{x,p_y,k}$$

of Λ_f in $\mathbb{R}^3$ with coordinates (x, p_y, k). Similarly to $\mathrm{emb}_v(\Lambda_{(m,h)})$ with $v = q, p$, the function K (2.10b) with value $k \in [-K_{\max}, K_{\max}]$ defines a Morse height function[10] for the image $\mathrm{emb}_u(\Lambda_f)$ of such an embedding. The difference being that on $\mathrm{emb}_v(\Lambda_{(m,h)})$, this function is trivial, i.e., all constant k-sections of $\mathrm{emb}_v(\Lambda_{(m,h)})$ have the same topology, while on $\mathrm{emb}_u(\Lambda_f)$ it is not: the $k = 0$ section is critical.

The embedding of Λ_f in $\mathbb{R}^3$ can be obtained directly by solving (2.10a) and (2.10b) for (y, p_x) and replacing them in (2.1). We proceed in a slightly different way. Notice that the value k of the $\mathrm{SO}(2)$ invariant K is conserved along the $\mathbb{S}^1$ trajectories of φ_{J_1} in (2.17) and therefore such trajectories define constant k-sections of either $\Lambda_{(m,h)}$ or Λ_f. In particular, constant k-sections $\gamma_1 = \Lambda_{(m,h)} \cap \{K(\mathbf{q}, \mathbf{p}) = k\} \subset \mathrm{T}^*\mathbb{R}^2$ can be defined as

$$\gamma_1 : \mathbb{S}^1 \to \mathbb{R}^4 : t \mapsto \mathbf{u}(t) \tag{2.32a}$$

with $t \in [0, 2\pi)$ and

$$\mathbf{u}(t) = \big(A_- \cos t,\ A_- \sin t,\ A_+ \cos(t + \alpha'),\ A_+ \sin(t + \alpha')\big)^T \tag{2.32b}$$

where $|k| \leq K_{\max}(m, h)$ in (2.16), the amplitudes are

$$A_\pm = \left(\sqrt{|f|^2 + 4k^2} \pm h\right)^{1/2} > 0, \tag{2.32c}$$

[10] Notice from (2.16) that $K_{\max} \approx R_{\max}$ when $R_{\max} \gg |f|$. This means that K in (2.10b) induces a suitable height function.

and the angle $\alpha' = \varphi_p - \varphi_q \in [0, 2\pi)$ in (2.23b) is such that

$$\cos(\alpha') = 2k/A_+ \quad \text{and} \quad \sin(\alpha') = m/A_+ \,. \tag{2.32d}$$

Notice that the phase shift α' is unambiguous for all (m,h,k) except $m = k = 0$. In the latter case, one of $A_\pm$ vanishes and we can set $\alpha' = 0$. Projecting (2.32) on the (x,y) or (p_x, p_y) planes gives circular constant k-sections of the embeddings of $\Lambda_{(m,h)}$ described in sec. 2.3.2 and illustrated in fig. 2, top. Projecting (2.32) on the (x, p_y) plane gives constant k-sections of u-embedded Λ_f in $\mathbb{R}^3$. We analyze the latter representation in more detail.

As shown in fig. 3(b) and (c), the two-dimensional surface $\mathrm{emb}_u(\Lambda_f) \subset \mathbb{R}^3$ obtained by using (2.32) to embed Λ_f with $f \neq 0$ in $\mathbb{R}^3$ with coordinates (x, p_y, k) is a cylinder over $\mathbb{S}^1$ whose one $\mathbb{S}^1$ section is collapsed into a closed interval λ_0 at $k = 0$. The surface $\mathrm{emb}_u(\Lambda_f)$ is smooth everywhere except at the end-points of λ_0 and has a self-intersection (i.e., normal crossing) along the interior of λ_0. We may call it a *squished cylinder*. For $f = 0$, λ_0 contracts to a point and $\mathrm{emb}_u(\Lambda_0)$ becomes a *pinched cylinder*. Comparing to fig. 3(a), we can see that λ_0 is the interleave segment of the Riemann surface S_f and that the end points of λ_0 are the branch points of that surface. It can also be seen that without the two branch points, the abstract Riemann surface S_f and its concrete realization $\mathrm{emb}_u(\Lambda_f)$ are diffeomorphic, and we can use the shorter notation S_f for both objects.

A path γ_2 on S_f that starts with $k < 0$ and ends with $k > 0$ crosses necessarily λ_0. When the crossing occurs at one of the branch points, the continuation is unambiguous; at all other points of λ_0, the path γ_2 continues *smoothly*. S_f is *orientable*. Indeed, its $k > 0$ and $k < 0$ halves of $\mathrm{emb}_u(\Lambda_f)$ are easily orientable cylinders. To relate their orientations, notice that the basis of a tangent 2-plane at a point of the $k < 0$ part can be translated continuously (and even smoothly) along γ_2 to the $k > 0$ part, see fig. 3(c). It follows that the two halves of $\mathrm{emb}_u(\Lambda_f)$ have opposite orientation in $\mathbb{R}^3$. To reflect this, we may call S_f a *squished cylinder with a twist*.

2.5 Hard wall reflection and gluing common level sets of H and J_1 into tori

We continue the analysis of the dynamics in $\mathrm{T}^*\mathbb{R}^2$ under Hamiltonian (2.1) by specifying what happens when a trajectory reaches the wall at $\rho = \rho_{\max}$ and reflects as illustrated in fig. 4(a). At this point, coordinates $\mathbf{q} = (x,y)$ with $\|\mathbf{q}\| = \rho_{\max}$ and (of course) angular momentum $J_1 = p_\phi$ remain unchanged, while the radial component p_ρ of conjugate momentum $\mathbf{p}$ changes sign, $p_\rho \mapsto -p_\rho$. From fig. 4(a) we can see that after reflection, the polar angle (2.5) remains unchanged, while its dual (2.22) jumps by the angle 2α, where $\alpha = \tan^{-1}(p_\rho/p_\phi) \in (0,\pi)$ is the angle between vector $\mathbf{p}$ and the tangent line to the boundary at the point of reflection $\mathbf{q}$. The reflection rule for the Cartesian components (p_x, p_y) of $\mathbf{p}$ is a rotation[11]

$$(\mathbf{q},\mathbf{p}) \mapsto (\mathbf{q}',\mathbf{p}') = \left(\mathbf{q}, S^{2\alpha}\,\mathbf{p}\right), \tag{2.33a}$$

with S^t in (2.2). Substituting into $\mathbf{q}' \wedge \mathbf{p}' = m$, we obtain (2.24) with $K_{\max} = K_{\max}(m,h)$ given in (2.16). We can now derive the reflection rules for invariants (2.8), (2.9), and (2.10)

$$(T,X,Y,J_1,K) \mapsto (T,X,Y,J_1,-K), \quad \text{when } R = R_{\max}. \tag{2.33b}$$

[11] Alternatively, reflection at a point $\mathbf{q}$ of the wall can be viewed as composition $\mathcal{T} \circ \sigma_{\mathbf{q}}$ where the axis of $\sigma_{\mathbf{q}}$ is given by vector $\mathbf{q}$.

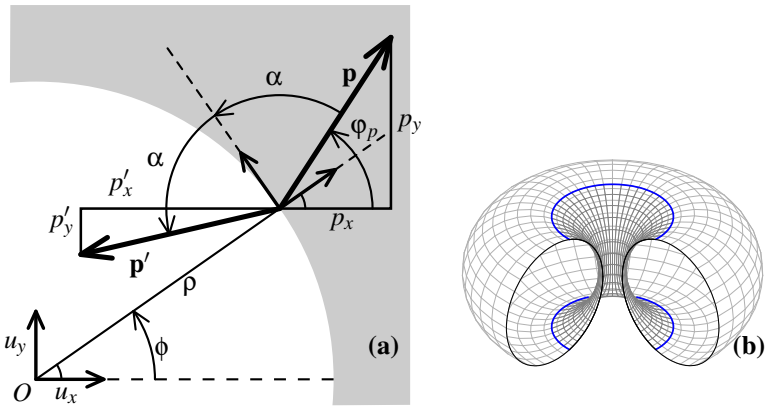

Figure 4: (a) Reflection rule for the Cartesian components of momentum $\mathbf{p} = (p_x, p_y)$ and $\mathbf{p}' = (p'_x, p'_y)$ before and after the impact respectively. (b) Possible immersion in $\mathbb{R}^3$ of a regular torus $\Lambda_{(m,h)}$ of the integrable fibration defined by (2.19) (dark) and its smooth analog (gray); the upper and lower circular edges (bold) are glued by the reflection rule (2.33a), cf. fig. 2, top.

The most important consequence of reflections (2.33) is that regular fibers in lemma 2.7 now become topological tori. This can also be seen after lifting the (m,h)-level sets of the reduced system back to $\mathrm{T}^*\mathbb{R}^2$, see sec. 2.7. Specifically, we have

Lemma 2.9 (Reconstruction)**.** *Due to reflections* (2.33)*, each regular* (m,h)*-level set* $\Lambda_{(m,h)}$ *of the energy-momentum mapping* (2.19) *is topologically a* 2*-torus. The critical set* $\Lambda_{(0,0)}$ *is a singly pinched torus.*

2.6 Motion in the full phase space $\mathrm{T}^*\mathbb{R}^2$

Solving the linear canonical equations of motion for the Hamiltonian H in (2.1)

$$\dot{\mathbf{u}} = (\dot{\mathbf{q}}, \dot{\mathbf{p}}) = (\mathbf{p}, \mathbf{q}), \tag{2.34}$$

gives the flow (2.18) for $\|\mathbf{q}\| < \rho_{\max}$, i.e., between reflections. We construct the general solution of (2.34).

2.6.1 Pericentre

As the particle moves up and down the potential (2.1b), the variable $X \geq 0$ changes in the interval $[X_{\min}, X_{\max}]$ reaching its maximum $X_{\max}$ in (2.16) at the wall. The point of the trajectory where X attains its minimum $X_{\min} \geq 0$ is called *pericentre* [31]. From (2.9) we see that at this point, both $\|\mathbf{q}\|$ and $\|\mathbf{p}\|$ are at their respective minima $q_{\min} = \rho_{\min} \geq 0$ and $p_{\min} \geq 0$ satisfying

$$|m| = q_{\min}\, p_{\min} \quad \text{and} \quad 2h = p_{\min}^2 - q_{\min}^2, \tag{2.35a}$$

which solve as

$$\rho_{\min}(m,h) = \sqrt{|f| - h} \quad \text{and} \quad p_{\min}(m,h) = \sqrt{|f| + h}. \tag{2.35b}$$

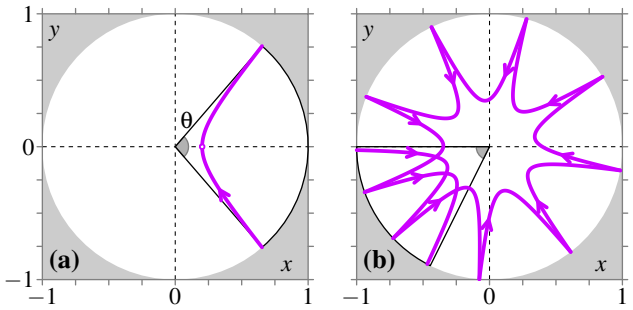

Figure 5: The $\mathbf{q}$-projection of trajectories (bold lines) of the system with Hamiltonian (2.1) and $\rho_{\max} = \sqrt{2}$. (a) A reference orbit (2.36) with $m > 0$, its pericentre (empty circle), and corresponding rotation angle θ (shaded segment at the origin). (b) A trajectory with $m = 0.1$ and $h = -0.1$, starting at the wall just below $x = -\rho_{\max}$, $y = 0$. The shaded segment at the origin indicates the total swept polar angle modulo 2π. Axes x and y are scaled in units of $\rho_{\max}$.

We see that for all $m \neq 0$, $\rho_{\min} > 0$ and the particle never reaches the origin—the fact well appreciated by those working in polar coordinates; see sec. 2.7.5. We also see from (2.11) that $X_{\min} \geq 0$ is attained when $K = \mathbf{q} \cdot \mathbf{p} = 0$, i.e., either when $\mathbf{q}$ and $\mathbf{p}$ are orthogonal, or when at least one of them is zero. It follows from (2.10b) that the former case corresponds to the turning point $p_\rho = 0$ of the radial motion.

2.6.2 Reference orbit, period of first return, and rotation angle

The particular trajectory reaching its pericentre with $\mathbf{q} = (x_0, 0)^T$ and $\mathbf{p} = (0, p_0)^T$ at time $t = 0$ will be called *reference orbit* [31]. The quantities x_0 and p_0 satisfy

$$x_0\, p_0 = m \quad \text{and} \quad p_0^2 - x_0^2 = 2h, \tag{2.35c}$$

so that $|x_0| = \rho_{\min}(m,h)$ and $|p_0| = p_{\min}(m,h)$. These equations are solved straightforwardly as

$$p_0 = \sqrt{2|f|}\,\cos\tfrac{1}{2}\arg(f) \quad \text{and} \quad x_0 = \sqrt{2|f|}\,\sin\tfrac{1}{2}\arg(f), \tag{2.35d}$$

which are continuous two-valued functions of f in (2.28). It follows from (2.18) that

$$\mathbf{u}(t) = S_H^t\, \mathbf{u}_0(m,h), \quad \text{with} \quad \mathbf{u}_0(m,h) = \big(x_0(m,h), 0, 0, p_0(m,h)\big)^T \tag{2.36}$$

defines the reference orbit.

Reference orbit (2.36) drawn in fig. 5(a) and fig. 2 for a particular value (m,h) illustrates two important characteristics of the flow φ_H on regular fibers $\Lambda_{(m,h)}$, namely the *period of first return* $\tau(m,h)$ and the *rotation angle* $\theta(m,h)$. A general geometric definition of θ and τ can be given as follows. Consider a point $\mathbf{u}'$ on $\Lambda_{(m,h)}$ and let $\gamma_1 \ni \mathbf{u}'$ be a periodic orbit of φ_{J_1} in (2.17),

$$\gamma_1 : [0, 2\pi) \to \mathbb{R}^4 : t \mapsto \varphi_{J_1}^t\, \mathbf{u}' = S_{J_1}^t\, \mathbf{u}_0.$$

A trajectory $\gamma : (t, \mathbf{u}') \mapsto \varphi_H^t \mathbf{u}'$ returns (for the first time) to γ_1 at point $\mathbf{u}'' = \varphi_H^{\tau(m,h)} \mathbf{u}' \neq \mathbf{u}'$ after time $\tau(m,h)$. On the other hand $\gamma_1 \ni \mathbf{u}'' = \varphi_{J_1}^{\theta(m,h)} \mathbf{u}'$, i.e., the flow φ_{J_1} reaches

$\mathbf{u}''$ in time $\theta(m,h)$. Because φ_{J_1} and φ_H commute, this definition of θ and τ does not depend on the point $\mathbf{u}'$. So for each regular fiber $\Lambda_{(m,h)}$, the quantity $\theta(m,h)$ gives the "twist" of the flow φ_H with respect to φ_{J_1}.

For all orbits γ_1 with $R \neq 0$, i.e., as long as $\|\mathbf{q}\| = \text{const} \neq 0$, and in particular for the orbit that goes along the wall with $R = R_{\max}$, the polar angle ϕ in (2.5) can serve as a natural coordinate along γ_1 because $\{\phi, J_1\} = 1$. So it can be seen that τ is the time that takes the reference orbit (2.36) starting at the wall to come back, i.e., the time between two bounces, while θ is the polar angle swept in the $\mathbf{q}$-plane during this time. It can also be seen that τ is the period of the radial motion. Explicit expressions for $\tau(m,h)$ and $\theta(m,h)$ are obtained in sec. 2.7.7.

2.6.3 General solution

The general solution to the equations of motion under Hamiltonian (2.1)

$$\mathbf{u}(t) = S_H^{t-t_0} S_{J_1}^{\phi_0} \mathbf{u}_0(m,h), \tag{2.37}$$

where S_H^t and $S_{J_1}^{\phi}$ are defined in (2.18) and (2.17), respectively, is parameterized conveniently by using the above particular solution (2.36) with $\mathbf{u}_0(m,h)$ and two additional phases defining the shift t_0 along the reference orbit and the rotation of the orbit as a whole by angle ϕ_0 about the origin. Notice that matrices S_H^t and $S_{J_1}^{\phi}$ commute and their sequence in (2.37) is unimportant. Notice also that the two parameters (m,h) appear only in $\mathbf{u}_0$.

An example of the trajectory (2.37) with $t_0 = \tau/2$ and $\phi_0 \approx \pi$ is provided in fig. 5(b). For all $q_{\min} < \rho_{\max}$, the motion is described by (2.37) as long as $\|\mathbf{q}\| < \rho_{\max}$. When the particle arrives at the wall and $\|\mathbf{q}\| = \rho_{\max}$, the reflection (sec. 2.5) makes the phases t_0 and ϕ_0 jump discontinuously by fixed quantities $\tau(m,h)$ and $\theta(m,h)$, respectively (sec. 2.7.7). The special case of $q_{\min} = \rho_{\max}$ is described in the next section.

2.6.4 Relative equilibria

There is a special class of trajectories of the system with Hamiltonian (2.1) that we have already described in sec. 2.3.1 as motions with constant $K = 0$. In this case, $|q_{\min}| = \rho_{\max}$. So, obviously, the particle remains at the wall with $\|\mathbf{q}\| = \rho_{\max}$ and $\mathbf{p}$ tangent to the wall. Consequently, $\|\mathbf{p}\| = p_{\min} = |m|$. Corresponding energy (2.15) follows from (2.35a). Furthermore, since in all other cases, we have either $0 < q_{\min} < \rho_{\max}$ and

$$h = \left(m^2 q_{\min}^{-2} - q_{\min}^2\right)/2 > h_{\min}(m),$$

or $q_{\min} = m = 0$ and again $h > 0 > h_{\min} = -\frac{1}{2}\rho_{\max}^2$, the energy $h_{\min}(m)$ is the minimal energy that can be attained by the particle with angular momentum m. The particle with energy $h_{\min}(m)$ moves along the circular hard wall if $m \neq 0$ or is at rest at some point at the wall if $m = 0$. Either the circular orbit that the particle follows or the set of all possible rest points constitute an $\mathbb{S}^1$ orbit of the $\mathrm{SO}(2)$ action (2.2). which is the *relative equilibrium* of the system. Since for sufficiently small $\delta > 0$, the trajectory with energy $h_{\min}(m) + \delta$ and momentum m remains near the relative equilibrium $\Lambda_{(m,h_{\min}(m))}$, the latter is stable. In a smooth analog system, it corresponds to an elliptic relative equilibrium.

2.7 Reduction of the axial SO(2) symmetry

In the previous sections, we studied the integrable fibration of the full phase space $\mathrm{T}^*\mathbb{R}^2$, and, in principle, we can continue—as Nekhoroshev would have done, analyzing monodromy at this level, cf. sec. 3. In this section, we *reduce* the $\mathbb{S}^1$ action (2.2) and so reduce the number of degrees of freedom to one. In more complex systems, such reduction of Lie symmetries (and of respective degrees of freedom) turns from convenience into necessity. Reduction of the non-free SO(2) action (2.2) (cf. remark 2.1) requires the technique of *singular* reduction [2–5, 58] which preserves the correct geometry of the system and is only slightly more involved technically than polar coordinates.

2.7.1 Momentum map

The momentum J_1 (2.10a) of the SO(2) action (2.2) defines the proper map

$$J_1 : \mathrm{T}^*\mathbb{R}^2 \to \mathbb{R} : \{(\mathbf{q},\mathbf{p}), J_1(\mathbf{q},\mathbf{p}) = m\} \to m.$$

The inverse image of $J_1^{-1}(m)$, or the m-level set of J_1, is the set of all orbits of (2.2) along which the value of J_1 equals m. It is a non-compact 3-dimensional subspace of $\mathrm{T}^*\mathbb{R}^2$. Note that $J_1^{-1}(m)$ for $m \neq 0$ are smooth, while $J_1^{-1}(0)$ has a singularity at $\mathbf{0} \in \mathrm{T}^*\mathbb{R}^2$ which is the critical orbit.

2.7.2 Explicit construction of orbit spaces using invariants

Orbit space of the SO(2) action Geometrically, reduction means descending from the total space $\mathrm{T}^*\mathbb{R}^2$ to the *orbit space* O, or the *orbifold* (in the sense of [46]) of the $\mathbb{S}^1$ action (2.2) of dimension

$$\dim O = \dim \mathrm{T}^*\mathbb{R}^2 - \dim \mathbb{S}^1 = 3.$$

The *reduction map* Π, which sends orbits $\mathbb{S}^1 \subset \mathrm{T}^*\mathbb{R}^2$ defined by (2.2) to points of O, is a bijection. The space O is non-compact and has a singular point representing the isolated critical orbit of the non-free action (2.2).

By the theorem of Chevalley [19], the orbits of a group action can be characterized fully by the values of invariants. Specifically [72, 46], all orbits can be labeled by the values of principal invariants and distinguished additionally using auxiliary invariants, if necessary. The invariant theory gives an explicit construction of O and P_m as *semi-algebraic varieties*, i.e., sets defined in terms of invariants through polynomial equalities and inequalities. We can label the orbits of the SO(2) action using allowed values of principal invariants X, Y, and K in (2.9) and (2.10). According to (2.11) with $J_1 = m \in \mathbb{R}$, the set O of all allowed values of these invariants is a union

$$O = O_{m<0} \cup P_0 \cup O_{m>0} = O_{m\leq 0} \cup O_{m>0} = O_{m<0} \cup O_{m\geq 0} \tag{2.38a}$$

of three sets of points $(X \geq 0, Y, K)$, such that

$$P_0 = \partial O_{m<0} = \partial O_{m>0} = \left\{(X,Y,K),\ X = (Y^2+K^2)^{1/2}\right\} \tag{2.38b}$$

is a straight cone and each of the sets $O_{m\geq 0}$ and $O_{m\leq 0}$ is a solid cone

$$O_{m\leq 0} = O_{m\geq 0} = \left\{(X,Y,K),\ X \geq (Y^2+K^2)^{1/2}\right\}. \tag{2.38c}$$

The whole orbit space O is obtained by gluing the two solid cones on their common boundary P_0. This gives a space $\mathbb{R}^3$ with singularity at the origin.

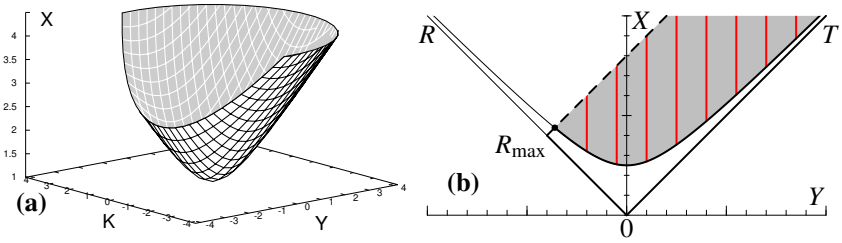

Figure 6: Embedding of regular reduced phase spaces P_m (2.39) and P_m^* (2.39*) with $m \neq 0$ in the ambient space $\mathbb{R}^3$ with coordinates (X,Y,K) (a) and its projection on the $\{K=0\}$ plane (b) with coordinate axes (Y,X) and rotated axes (R,T). Dashed line marks the 'wall' $R = R_{\max}$ and shaded area indicates the part of the space allowed by $R < R_{\max}$, red lines represent constant level sets of reduced Hamiltonian (2.14).

Orbit space of the $\mathrm{O}(2)$ action Momentum J_1 is a covariant of the $\mathrm{O}(2)$ action whose orbits can be labeled by m^2 or $|m|$. For $m \neq 0$, each such orbit is a disjoint union of two $\mathbb{S}^1$ orbits of (2.2a) with opposite signs of J_1. It follows that the orbit space of the $\mathrm{O}(2)$ action is a solid cone (2.38c).

2.7.3 Geometry of the reduced phase space P_m

Under the reduction map Π, orbits of the $\mathrm{SO}(2)$ action (2.2) with given value m of first integral J_1 map bijectively to points of the reduced phase space $P_m \subset O$ of dimension 2. So, on the one hand, P_m is an image of $J_1^{-1}(m)$ under Π, and on the other, it is a constant-m section of O. In fact J_1 defines a Morse height function on O with critical section P_0. The latter has one singular point representing the isolated critical orbit; all other spaces P_m with $m \neq 0$ are smooth. This is an illustration of the general distinctive feature of singular reduction: depending on m, the reduced phase spaces may have different geometries, and some of them are singular.

Quadratic form $\Phi(X,Y,K)$ in (2.11) is, to a factor, an expression of the square of the auxiliary invariant J_1^2 in terms of (X,Y,K). So slicing the orbit space O of the $\mathrm{SO}(2)$ action by the a constant level set of $\Phi(X,Y,K)$ selects all $\mathrm{SO}(2)$ orbits with given m and gives P_m. Specifically,

$$P_m = \{\Phi(X,Y,K) = \tfrac{1}{8}m^2\} \cap \begin{array}{ll} O_{m\geq 0}, & \text{for } m \geq 0, \\ O_{m\leq 0}, & \text{for } m \leq 0, \end{array}$$

and we obtain

$$P_m := \left\{(X \geq 0, Y, K),\ 2\,\Phi(X,Y,K) = X^2 - Y^2 - K^2 = \tfrac{1}{4}m^2\right\}. \tag{2.39}$$

Using this definition, P_m can be immersed properly in $\mathbb{R}^3$ with coordinates (X,Y,K). For $m \neq 0$, this gives an upper sheet of a circular two-sheet hyperboloid shown in fig. 6(a), which for $m = 0$, degenerates into a straight half-cone.

We can now detail the restrictions on the invariants in (2.8) and (2.9) by noticing that the surface (2.39) has a global minimum at

$$(X,Y,K) = (\tfrac{1}{2}|m|, 0, 0) \tag{2.40}$$

at which $T = R = X$, and therefore

$$X \geq \tfrac{1}{2}|m| \quad \text{and} \quad R \geq \tfrac{1}{2}|m|. \tag{2.41}$$

Remark 2.10. Going back to sec. 2.6, one may notice that the SO(2) orbit represented by (2.40) is the set of all pericentres for a particular value of energy $h = 0$. Restriction (2.41) is, however, of a general nature, a consequence of the SO(2) symmetry not related to the particular Hamiltonian.

Fully reduced space We do not reduce reversal symmetry $\mathcal{T}$ because it is not symplectic; the reduced system inherits it. However, the space of orbits of $\mathrm{O}(2) \times \mathcal{T}$ with given fixed value m of angular momentum J_1, or the *fully reduced space*, can be useful. This space may be denoted $P_m/\mathbb{Z}_2$, a factor by the order-2 group $\mathbb{Z}_2 = \{1, \mathcal{T}\}$. From (2.13), we can see that the action of $\mathcal{T}$ on P_m has two-point generic orbits with $K \neq 0$, which map to one point in $P_m/\mathbb{Z}_2$. So the latter can be constructed by projecting P_m on the plane (X, Y), see fig. 6(b).

2.7.4 Consequences of hard wall reflections

When reducing the compactified motions which include reflections at the wall $\|\mathbf{q}\| = \rho_{\max}$, we have to further account for (2.12) by removing the large-R parts of O and P_m. We obtain

$$O^*_{m\geq 0} := \left\{(X,Y,K),\ 0 \leq (Y^2+K^2)^{1/2} X \leq R_{\max} + Y\right\}, \tag{2.38c*}$$

$$P^*_m := \left\{(X,Y,K),\ 2\Phi(X,Y,K) = \tfrac{1}{4}m^2,\ 0 \leq X \leq R_{\max} + Y\right\}. \tag{2.39*}$$

So, in particular, the reduced phase space P^*_m has a slanted cut illustrated in fig. 6, where $|K|$ attains its maximum $K_{\max}$ in (2.16b). Furthermore, according to the rule (2.33b), the space P^*_m is glued along the cut $\{X - Y = R_{\max}\}$ by identifying points $(X,Y,K) = (R_{\max} + Y, Y, \pm K_{\max})$.

2.7.5 Description in polar coordinates

The apparent simplicity of polar canonical coordinates (see sec. 2.2.1) is that in these coordinates, the Hamiltonian (2.1)

$$H(\rho,\phi,p_\rho,p_\phi) = H(\rho,p_\rho,p_\phi) = \frac{1}{2\mu}\left(p_\rho^2 + p_\phi^2/\rho^2\right) - \frac{a}{2}V(\rho), \quad \rho \geq 0, \tag{2.42}$$

does not depend on the polar angle ϕ in (2.5). So, ϕ is an ignorable variable and we can immediately reduce the system with Hamiltonian (2.42) by treating the conserved momentum $p_\phi = J_1 = m$ as a parameter. The resulting reduced *radial* Hamiltonian

$$H_m(\rho,p_\rho) = \frac{1}{2\mu}\left(p_\rho^2 + m^2/\rho^2\right) - \frac{a}{2}V(\rho) = \tfrac{1}{2}\left(p_\rho^2 + m/\rho^2\right) - \tfrac{1}{2}V(\rho), \tag{2.43}$$

is studied commonly in standard textbooks on mechanics. What is much less acknowledged, is the complication in the case $m = 0$, where polar coordinates do not represent adequately the orbits of the SO(2) action (2.2). We explain this in more detail.

We saw in sec. 2.7.3 that (without restriction $\|\mathbf{q}\| \leq \rho_{\max}$) the reduced phase space P_m, or the space of orbits of the SO(2) action with a given value m of momentum $J_1 = p_\phi$, has the topology of $\mathbb{R}^2$. Furthermore, for all m this space can be mapped bijectively to the plane $\mathbb{R}^2$ with coordinates (Y,K). As illustrated in fig. 6(a), the map is a simple projection; it is a diffeomorphism for all $m \neq 0$ and for all $(Y,K) \neq 0$ in the case of $m = 0$.

On the other hand, describing the same space using polar coordinates (ρ, p_ρ) is similar to using invariants (R,K) instead of (Y,K); cf. eqs. (2.8a) and (2.10b). We can clearly see from fig. 6(b) that for $m \neq 0$, this representation results necessarily in a considerable distortion of the region of P_m with small R and K, and for $m = 0$, it blows up on the line $\{R = K = 0, T > 0\} \subset P_0$, i.e., the positive semiaxis T. The image of the latter in the (ρ, p_ρ) space is axis p_ρ without the origin $\{(\rho, p_\rho), \rho = 0, p_\rho \neq 0\}$.

The obvious advantage of (ρ, p_ρ) is that these are globally symplectic coordinates on $\mathbb{R}^2$ equipped with a standard symplectic 2-form $\mathrm{d}\rho \wedge \mathrm{d}p_\rho$ and that the radial Hamiltonian (2.43) can be defined formally on the same phase space regardless of m. So we can study the radial motion using "standard" Hamiltonian equations of motion for a system with one degree of freedom. However, as the above comparison with P_m shows, this $\mathbb{R}^2$ should be "folded" in a special way in order to reproduce correctly the set of all $\mathrm{SO}(2)$ orbits and the resulting radial phase space is singular. Physicists accomplish this by exploiting the dynamics of the system.

For $m \neq 0$, the singularity at $\rho = 0$ may be regarded as "not important" because the special additional term $(m/\rho)^2$ in $H_m(\rho, p_\rho)$ prevents trajectories from reaching the origin. Specifically, the motion takes place between the inner turning point at $\rho = \rho_{\min} = \rho_-(m,h)$ and the wall at $\rho_{\max}$, where

$$\rho_\mp^2(m,h) = \frac{\mp\mu h + \sqrt{(\mu h)^2 + a\mu m^2}}{a\mu} = \mp h + \sqrt{h^2 + m^2} \geq 0$$

is strictly positive for $m \neq 0$. The particle approaches the origin $\mathbf{q} = 0$ with $p_\rho < 0$ and goes away from $\mathbf{q} = 0$ with $p_\rho > 0$. The absolute value of p_ρ is given by

$$p_\rho^2 = 2\mu\left(h + \frac{a}{2}\rho^2 - \frac{m^2}{2\mu\rho^2}\right) = a\mu\frac{(\rho^2 - \rho_-^2)(\rho^2 + \rho_+^2)}{\rho^2}.$$

So it follows that the radial phase space for any $m \neq 0$ can be taken as an open half-plane $\{p_\rho, \rho > 0\}$ and is diffeomorphic to $\mathbb{R}^2$.

For $m = 0$, the particle moves along straight radial lines in the $\mathbf{q}$-space. With regard to h, there are two qualitatively different structurally stable trajectories with $h < 0$ and $h > 0$. The former have again a turning point at $\rho_- > 0$, and are similar to the case $m \neq 0$ above, albeit ϕ remains constant. The latter have $\rho_-(0,h) = 0$, $\rho_+(0,h) = 2h$, and there is no turning point. So, as it goes through the origin the radial momentum p_ρ *jumps* from $p_\rho = +\rho_+$ to $p_\rho = -\rho_+$ (and ϕ also jumps by π). This means that the $\mathbb{R}^2$ phase phase space of (2.43) becomes a half plane $\{p_\rho, \rho \geq 0\}$ whose positive and negative semiaxes p_ρ are identified yielding a cone. If the local symplectic structure is deformed correctly, the seam on the cone should disappear and we should obtain P_0.

2.7.6 Dynamics of the reduced system

After reduction of the $\mathrm{SO}(2)$ action, we obtain a Hamiltonian dynamical system with one degree of freedom on the two-dimensional reduced phase space P_m. The reduced dynamics is described using the Poisson algebra generated by the $\mathrm{SO}(2)$ invariants. This is known as Euler-Poisson reduction. Expressing the original Hamiltonian $H(\mathbf{q}, \mathbf{p})$ in (2.1) as function of invariants and replacing J_1 by its value m, which now becomes a parameter, gives the *reduced Hamiltonian* $\mathcal{H}_m(X,Y,K)$ that in our simple case (2.14) does not even depend on m and will be denoted $\mathcal{H}$.

Reduced trajectories Trajectories of the motion under $\mathcal{H}$ on the two-dimensional space P_m^* (the space P_m which is cut off to $R \le R_{\max}$ due to the wall reflection) are given by the h-level sets of $\mathcal{H}$ on P_m^*. In the ambient space $\mathbb{R}^3$ they are obtained as

$$\lambda_{(m,h)} := \{(X,Y,K), \mathcal{H} = h\} \cap P_m^* = \left\{Y = \tfrac{1}{2}h\right\} \cap P_m^*, \tag{2.44a}$$

where we used $\mathcal{H} = H$ in (2.14). From (2.39*) and (2.16b) we obtain

$$\lambda_{(m,h)} = \left\{ (X,Y,K), |K| \le K_{\max}(h),\ Y = \tfrac{1}{2}h,\ X = \sqrt{\tfrac{1}{4}|f|^2 + K^2} \right\}. \tag{2.44b}$$

To finalize the construction, recall from sec. 2.7.4 that the points of P_m^* on the $R = R_{\max}$ hard wall cutoff are identified. So we identify the two endpoints

$$(X,Y,K) = \left(X_{\max}, \tfrac{1}{2}h, \pm K_{\max}\right) \tag{2.45}$$

of the closed interval (2.44b). It follows that the level set $\lambda_{(m,h)}$ of the reduced Hamiltonian $\mathcal{H}$ is topologically a circle $\mathbb{S}^1$. This level set is smooth everywhere except for the point represented by the endpoints (2.45).

Trajectories (2.44b) are shown in fig. 6(b) projected on the (X,Y) plane. It can be seen that

$$X_{\min} = \tfrac{1}{2}|f|, \quad R_{\min} = \tfrac{1}{2}(X_{\min} - h), \quad T_{\min} = \tfrac{1}{2}(X_{\min} + h),$$

while at the same time

$$R_{\max} = \tfrac{1}{2}\rho_{\max}^2, \quad T_{\max} = R_{\max} + h, \quad X_{\max} = R_{\max} + \tfrac{1}{2}h.$$

Reduced equations of motion Dynamics on P_m is described using the Poisson algebra generated by principal invariants (X,Y,K). This algebra can be computed using the original symplectic coordinates $(\mathbf{q},\mathbf{p})$ and definitions (2.9) and (2.10). We obtain

$$\{X,Y\} = K, \quad \{Y,K\} = -X, \quad \{K,X\} = Y, \tag{2.46a}$$

which has the structure of $\mathrm{so}(2,1)$ and is reproduced compactly by the Dirac's formula

$$\{a,b\} = -\varepsilon_{abc}\,\partial\Phi(X,Y,K)/\partial c. \tag{2.46b}$$

Here Φ defines the relation (2.11) between (X,Y,K) and ε_{abc} is the sign of permutation (abc) of (X,Y,K). Momentum J_1 (and, naturally, Φ) is the Casimir. We can now write down the equations of motion for $\mathcal{H} = H$ in (2.14)

$$(\dot{X},\dot{Y},\dot{K}) = \{(X,K,Y), \mathcal{H}\} = 2\,(K,0,X). \tag{2.47}$$

Remark 2.11. Because the $\mathrm{SO}(2)$ group action (2.2) commutes with derivation, the Poisson bracket of two smooth invariant functions F_1 and F_2 is itself a smooth invariant function. So if F_1 and F_2 Poisson commute with the infinitesimal generator J_1 of (2.2), then $\{F_1,F_2\}$ also commutes with J_1. This also follows from (2.46b) or the Jacobi identity for $\{\{F_1,F_2\},J_1\}$. If F_1 and F_2 belong to the polynomial ring generated by (X,Y,K), their bracket is also a polynomial in (X,Y,K).

Remark 2.12. Because Φ defines the reduced phase space P_m in (2.39) and is a Casimir of (2.46), the vector field (2.47) is tangent to P_m and the Euler-Poisson equations leave P_m invariant. This holds for *any* Hamiltonian $\mathcal{H}(X,Y,K)$ since $\{\Phi,\mathcal{H}\} = 0$.

Solving (2.47) we obtain the reduced linear flow

$$\varphi^t_{\mathcal{H}} : \mathbb{R}\times\mathbb{R}^3 \to \mathbb{R}^3 : (t,(X,Y,K)^T) \mapsto S^t_{\mathcal{H}}(X,Y,K)^T \tag{2.48}$$

of $\mathcal{H}$ with

$$S^t_{\mathcal{H}} = \begin{pmatrix} \cosh 2t & 0 & \sinh 2t \\ 0 & 1 & 0 \\ \sinh 2t & 0 & \cosh 2t \end{pmatrix}$$

By remark 2.12, this flow preserves P_m and can therefore be naturally restricted on it. Of course, (2.48) applies only while $R(t) = X(t) + h/2 \le R_{\max}$. To describe the reduced dynamics completely we must also account for the reflections at $R = R_{\max}$ and $K = \pm K_{\max}$. With these reflections, the motion on P_m becomes periodic with period $\tau(m,h)$. So we can parameterize the reduced orbit (2.44b) of (2.48) by

$$t = \tau(m,h)\,\xi \quad \text{with } \xi \in [-\tfrac{1}{2},\tfrac{1}{2}],$$

such that for $t = \xi = 0$, we begin with $X(0) = X_{\min}$ and $K(0) = 0$ and from (2.48) we have

$$X(t) = X_{\min}\cosh 2t, \quad K(t) = X_{\min}\sinh 2t, \quad Y = \tfrac{1}{2}h, \quad \text{and} \quad J_1 = m.$$

Notice[12] that in the full space $\mathbb{R}^4$, this corresponds to starting the trajectory in (2.36) and (2.37) at its pericentre (sec. 2.6.1).

2.7.7 First return time τ and rotation angle θ

The period of first return $\tau(m,h)$ and the rotation angle $\tau(m,h)$ introduced in sec. 2.6.2 are central to the construction of the second action variable J_2, the second basis cycle $[\gamma_2]$ of $H_1(\Lambda_{(m,h)})$ in sec. 3.1 and to the analysis of monodromy in sec. 3.3. There are various ways to compute these quantities easily from the explicit general solution for our system (2.37). All methods, however, lead necessarily to $\mathrm{SO}(2)$-invariant integrals, and so can be best understood in terms of reduced dynamics.

On the reduced phase space P_m, the reduced orbits (2.44b) given by the reduced flow (2.48) are closed, i.e., the reduced motion begins at and returns back to a point on P_m which lifts to an $\mathbb{S}^1$ orbit of the $\mathrm{SO}(2)$ action (2.2) and (2.17). So it follows directly from its definition in sec. 2.6.2 that $\tau(m,h)$ is the period of the reduced motion. Using (2.47) and the fact that reduced trajectories on P_m go from $X = X_{\max}$ (and $K = -K_{\max}$) to $X = X_{\min}$ (and $K = 0$) and then back to $X = X_{\max}$ (and $K = K_{\max}$), we compute

$$\tau(m,h) = \int_0^\tau \mathrm{d}t = \int_{X(0)}^{X(\tau)} \frac{\mathrm{d}X}{2K} = \int_{X_{\min}}^{X_{\max}} \frac{\mathrm{d}X}{K} = \int_{X_{\min}}^{X_{\max}} \frac{\mathrm{d}X}{\sqrt{X^2 - X^2_{\min}}}, \tag{2.49}$$

where we integrate $\mathrm{d}X$ only for the $K \ge 0$ half of the orbit.

Remark 2.13. In polar coordinates, the same calculation begins with integrating $\mathrm{d}t = \mathrm{d}\rho/\dot\rho$ over the period of the radial motion. Rewriting the integrand as $\mathrm{d}R/\dot R = \mathrm{d}X/\dot X$ we come to (2.49). This illustrates the general situation of computing τ and θ. In more complicated cases, working directly from within the reduced Euler-Poisson system gives a clearer advantage.

[12] The $\mathbb{S}^1$ orbit of φ_{J_1} labeled by $(J_1,X,Y,K) = (m, X_{\min}, \frac{1}{2}h, 0)$ with $(m,h) \notin \{m = 0, h \ge 0\}$ goes through all possible pericentres and bounds the inaccessible domain in the $\mathbf{q}$-space.

The polar angle $\varphi_q = \phi$ or the dual angle φ_p are not in the reduced system. However, their evolution is driven by the reduced dynamics and the time derivatives $\dot{\varphi}_q$ and $\dot{\varphi}_p$ are functions on P_m that are well defined when the corresponding q and p-embeddings are regular, i.e., away from $\{m=0, h\geq 0\}$ and $\{m=0, h\leq 0\}$, respectively (sec. 2.3.2). A direct calculation with Hamiltonian (2.14) gives

$$\dot{\varphi}_q = \left\{\tan^{-1}\frac{y}{x}, H\right\} = \frac{J_1}{2R} = \frac{J_1}{2(X-Y)} = \frac{m}{2X-h}$$

and (the less familiar)

$$\dot{\varphi}_p = \left\{\tan^{-1}\frac{p_y}{p_x}, H\right\} = -\frac{J_1}{2T} = -\frac{J_1}{2(X+Y)} = -\frac{m}{2X+h}.$$

Proceeding similarly to the calculation of τ (2.49), i.e., integrating between two bounces of (2.37) and using relation $\mathrm{d}X = \mathrm{d}R = 2K\,\mathrm{d}t$, we find that polar angle $\varphi_q \in [0, 2\pi)$ changes in time τ by

$$\theta(m,h) = \frac{m}{2}\int_{X_{\min}}^{X_{\max}} \frac{\mathrm{d}X}{(X-h/2)\sqrt{X^2-X_{\min}^2}}. \tag{2.50}$$

Integration of (2.49) and (2.50) gives explicit expressions of τ and θ as smooth real functions on the set $\mathbb{R}^2 \setminus 0$ of regular (m,h) values. The period τ is a single-valued function with logarithmic singularity at $(m,h)=0$,

$$\tau(m,h) = \cosh^{-1}\frac{2X_{\max}}{|f|} = \cosh^{-1}\frac{2R_{\max}+h}{|f|} = \sinh^{-1}\frac{2K_{\max}}{|f|}, \tag{2.51a}$$

$$\tau(m,h) \approx \log 4R_{\max} - \log|f| + \dots \quad \text{when } 0 < |f| \ll R_{\max}. \tag{2.51b}$$

Here various forms in (2.51a) follow from (2.16) and equality $\sinh\left(\cosh^{-1}x\right) = \sqrt{x^2-1}$. The rotation angle θ is a *multivalued* function

$$\theta(m,h) = 2\tan^{-1}\left(\frac{h+|f|}{m}\sqrt{\frac{2R_{\max}+h-|f|}{2R_{\max}+h+|f|}}\right), \tag{2.52a}$$

which has an asymptotic form

$$\theta(m,h) \approx \pi - \arg(f) + \dots \quad \text{when } 0 < |f| \ll R_{\max}. \tag{2.52b}$$

This multivaluedness of θ can be seen as the origin of monodromy.

Remark 2.14. Asymptotic expressions (2.51b) and (2.52b) are common to focus-focus (complex unstable or complex hyperbolic) equilibria of integrable Hamiltonian dynamical systems with two degrees of freedom [69]. This extends to originally non-integrable systems normalized and truncated near such equilibria. Universality of such expressions leads to the statement that all systems with a focus-focus equilibrium have the same 'elementary' monodromy, and, eventually, to the "geometric monodromy theorem" of [24]. As we explain in sec. 2.4 and 3, it is the Hamiltonian equivalent of the Picard-Lefschetz monodromy of the Morse singularity A_1.

2.8 Smooth analogs of the hyperbolic circular billiard

Our linear system with trajectories described by elementary functions gives a rare opportunity to compute everything explicitly. Furthermore, similarly to the A_1 singularity, we can employ the Morse lemma and normal form arguments to make this system a universal model, an asymptotic approximation to what happens in *any* particular nonlinear system with a focus–focus equilibrium. In nonlinear systems that we briefly discuss here, explicit closed form general solutions of equations of motion involve—at best—parametric families of elliptic functions. Using these solutions in order to compute the period τ and the rotation angle θ as functions of (m,h) (cf. sec. 2.7.7), construct cycles (cf. sec. 3.1) and local actions (cf. sec. 5) can be much more demanding.

The direct smooth analog of the billiard with Hamiltonian (2.1) is the system where the infinite wall at $\rho_{\max}$ in (2.1b) is replaced by a positive-definite axially symmetric function $R(\mathbf{q}) = O(\rho^k)$ with $k > 2$, such as the system with the "champagne bottle" or "Mexican hat" potential

$$V(\mathbf{q}) = -\frac{a}{2}\,\|\mathbf{q}\|^2 + b\,\|\mathbf{q}\|^4 = O(\rho^4) \quad \text{with } a,b > 0,$$

resulting in smooth compactifaction of fibers as shown in fig. 4(b). The base of the integrable fibration of this system is equivalent to the one in fig. 1. Its monodromy was reported early by Bates [15] and was described later in a large class of concrete physical systems, rotating and bending quasi-linear molecules [73].

A symplectic rotation of $T^*\mathbb{R}^2$ by $\pi/4$ turns (2.10a) into a $1{:}-1$ resonant harmonic oscillator Hamiltonian. After a proper compactification [48], the latter defines an integrable system with a focus-focus equilibrium. The base of the fibration in that system is same as $\bar{\mathsf{R}}$ in fig. 1. From this we can conclude that the singularities of the two systems and the fibrations in their neighbourhoods are equivalent.

More generally, it can be shown [69] that the integrable fibration in a (sufficiently large) regular open neighbourhood of any nondegenerate focus-focus equilibrium is qualitatively equivalent to the one in sec. 2.3.2. Furthermore, in such neighbourhoods, one of the actions on regular fibers can be made global and thus turned into a momentum J_1. In other words, we can impose an $\mathbb{S}^1$ symmetry throughout the neighbourhood [55]. (The argument parallels the description of the Morse singularity A_1.) As already suggested in remark 2.14, asymptotic results are the same for all focus-focus points and for the singularity in our system.

3 Homology cycle bases on regular fibres. Hamiltonian and Picard–Lefschetz monodromy

The idea of the analysis in our Hamiltonian setup and in the Picard–Lefschetz theory is to study the monodromy of the family of regular fibres Λ. All these fibres have the same topology, and in particular, their first homology groups $H_1(\Lambda)$ are isomorphic. However, they fit together in a nontrivial way. More precisely, the fibre bundle over R (the set of regular values of $\mathcal{EM}$) is nontrivial. To demonstrate that and to characterize the nontriviality, one studies the *monodromy map* μ from the fundamental group $\pi_1(\mathsf{R})$ to the group of orientation preserving automorphisms of $H_1(\Lambda)$. In our case with two degrees of freedom and orientable base $\bar{\mathsf{R}}$, and with regular fibres $\Lambda \sim \mathbb{T}^2$, this latter

group is (isomorphic to) the group[13] $\mathrm{SL}(2,\mathbb{Z})$, and therefore

$$\mu : \pi_1(\mathsf{R}) \to \mathrm{SL}(2,\mathbb{Z}).$$

This map is defined as follows. In the base R of the bundle, for each homotopy class $[\Gamma]$ of $\pi_1(\mathsf{R})$, we consider a closed directed loop $\Gamma \subset \mathsf{R}$ representing $[\Gamma]$. For a point $\mathbf{s}_0 \in \Gamma$, we consider the fibre $\Lambda_{\mathbf{s}_0}$ and its homology $H_1(\Lambda_{\mathbf{s}_0})$. Because the bundle is *locally trivial*[14], the cycles of $H_1(\Lambda_{\mathbf{s}})$ can be redefined continuously in $\mathbf{s}$ when the latter follows along Γ. So for any two sufficiently close points $\mathbf{s}'$ and $\mathbf{s}''$ on Γ this gives an explicit isomorphism $H_1(\Lambda_{\mathbf{s}'}) \to H_1(\Lambda_{\mathbf{s}''})$, and as we return to $\mathbf{s}_1 = \mathbf{s}_0$ we obtain the automorphism $\mu_{\Gamma,\mathbf{s}_0} : H_1(\Lambda_{\mathbf{s}_0}) \to H_1(\Lambda_{\mathbf{s}_1})$, which is called *monodromy transformation*, and which depends neither on the choice of the particular Γ within $[\Gamma]$ nor on the choice of the particular point $\mathbf{s}_0$:

$$\mu_{[\Gamma]} : H_1(\Lambda) \to H_1(\Lambda).$$

This transformation is defined by a matrix $M_{[\Gamma]} \in \mathrm{SL}(2,\mathbb{Z})$ whose *rows* represent the new basis elements.

In our case, R is an open punctured half-plane, see fig. 1 and sec. 2.3.2. We define the nontrivial, i.e., non-contractible, loop

$$\Gamma : [0,60] \to \mathsf{R} \subset \mathbb{R}^2 : s \mapsto \begin{pmatrix} m(s) \\ h(s) \end{pmatrix} = \begin{pmatrix} \sin \Omega s \\ -\cos \Omega s \end{pmatrix} \quad \text{with } \Omega = 2\pi/60, \tag{3.1}$$

which goes around the isolated critical value $(0,0)$, see fig. 7(a), and whose points are specified in "minutes" $0' \ldots 60'$, see fig. 7(b). This notation originates in [32, 31, cf. footnote 3]. Γ is often called *contour* or *monodromy circuit*. By convention [21, see footnote 7], axes m and h are horizontal and vertical, respectively, and the positive direction on Γ is counterclockwise.

Theorem 3.1 (Monodromy of the fibration defined by H and J_1)**.** *The monodromy transformation $\mu_{[\Gamma]}$ for the homotopy class $[\Gamma] \in \pi_1(\mathsf{R})$ represented by the non-trivial circuit $\Gamma \in \mathsf{R}$ in (3.1) and fig. 7 defines the monodromy map μ for the integrable fibration in sec. 2.3.2 which is associated with Hamiltonian functions J_1 (2.10a) and H (2.1). The transformation $\mu_{[\Gamma]}$ is given by a matrix in the conjugacy class of*

$$M_\pm = \begin{pmatrix} 1 & 0 \\ \mp 1 & 1 \end{pmatrix} \in \mathrm{SL}(2,\mathbb{Z}), \tag{3.2}$$

where M_+ and M_- refer to positive and negative directions on $[\Gamma]$.

Remark 3.2. Matrix (3.2) is often called *monodromy matrix*. It depends, obviously, on the choice of the initial cycle basis $\{[\gamma_1],[\gamma_2]\}_{s=0'}$ and consequently, it is defined up to a conjugation in $\mathrm{SL}(2,\mathbb{Z})$.

Proof. The set R of regular values of the energy-momentum map $\mathcal{EM}$ defined by H and J_1 is not simply connected and is homotopic to a circle $\mathbb{S}^1$, see fig. 7(a). So like that of $\mathbb{S}^1$, the fundamental group $\pi_1(\mathsf{R})$ of R is (isomorphic to) $(\mathbb{Z},+)$. It is generated by the class $[\Gamma]$ of nontrivial loops Γ that encircle *once* the isolated critical value $(0,0)$,

[13] Matrices $M \in \mathrm{SL}(2,\mathbb{Z})$ have $\det M = +1$. For more general fibrations, one may have to allow for any change of cycle directions and use $M \in \mathrm{GL}(K,\mathbb{Z})$ with $\det M = \pm 1$.

[14] In the Hamiltonian setup, the Liouville-Arnol'd theorem ensures the existence of local angle-action variables that define local trivialization.

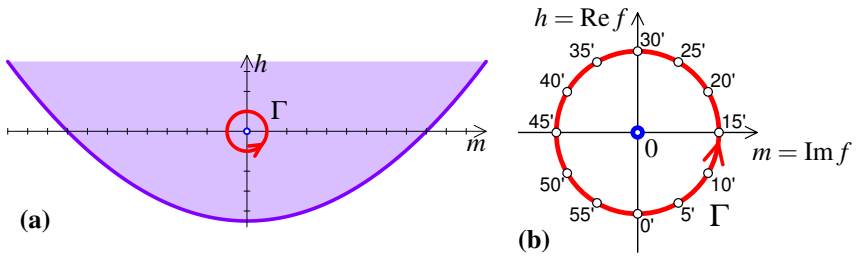

Figure 7: Monodromy circuit or "contour" Γ (bold directed circle) around the isolated critical value $(0,0)$ in the image of the energy-momentum map $\mathcal{EM}$ of the system with Hamiltonian (2.1) and $\rho_{\max} = 3$: (a) Γ as defined in (3.1) lies within the set R of regular $\mathcal{EM}$ values, cf. fig. 1; (b) snapshot points on Γ in units of $s \in [0,60]$ used in [32].

such as (3.1). Therefore, in order to find the monodromy map μ, it is necessary and sufficient to find the automorphism $\mu_{[\Gamma]}$ corresponding to this loop.

To find $\mu_{[\Gamma]}$, we compute continuously a basis $\{[\gamma_1],[\gamma_2]\}$ in $H_1(\Lambda_{(m(s),h(s))})$, for each $(m(0),h(0)) \in \Gamma$ as defined by (3.1) and beginning in $(m(0),h(0))$. To represent the first cycle $[\gamma_1]$, we take the integral curve γ_1 of X_{J_1}. The second cycle $[\gamma_2]$ has to be constructed. This is done in two different ways.

In sec. 3.1, we construct γ_2 using parts of the integral curves of X_H and X_{J_1} followed to time $\tau(m(s),h(s))$ and combined so that the result is a specific closed loop on $\Lambda_{(m(s),h(s))}$. This relies heavily on the dynamical study in sec. 2.5, 2.6, and 2.7.7. Alternatively, following the method of Nekhoroshev in sec. 4, we construct γ_2 directly from the geometry of the common level sets of H and J_1 and we exploit the dynamics *only* to define the directions of the cycles. For our particular choice of the cycle basis, taking the positive direction on (3.1) and comparing cycles in $s = 0$ to their continuation in $s = 60'$, we find M_+ in (3.2), see sec. 3.3.

A different (third) proof can be obtained by exploiting the relation of the fibration under study to the A_1 singularity (sec. 2.4) and applying the Picard-Lefschetz theory. In the A_1 case, γ_2 does not have to be constructed explicitly, and its variation over Γ is obtained geometrically as explained in sec. 3.4. This resembles in many ways the Nekhoroshev's approach in sec. 4. In order to demonstrate the complete equivalence to the Hamiltonian case, we take the Hamiltonian cycles constructed in sec. 3.1 and transfer them to the complex case using the isomorphism Ψ (2.25). We show how these cycles can be made suitable for the Picard-Lefschetz theory.[15] □

Nontrivial monodromy has important consequences. Because of it, the classical system with Hamiltonian (2.1) cannot have global action variables $\{J_1,J_2\}$ defined smoothly for all $(m,h) \in$ R and the corresponding quantum system does not have global quantum numbers (sec. 5).

3.1 Basis cycles of $H_1(\Lambda_{(m,h)})$

One of the cycles, which we call $[\gamma_1]$, can be defined *globally* on all fibres $\Lambda_{(m,h)}$ using orbits of the SO(2) action (2.2) or, equivalently, the orbits of the flow (2.17). This natural choice is standard for any system with global momenta and, more generally,

[15] All figures in sec. 3.2 and 3.4 that illustrate the Picard-Lefschetz theory are computed using our explicit Hamiltonian definitions of $\{[\gamma_1],[\gamma_2]\}$ in sec. 3.1 and the isomorphism Ψ (2.25).

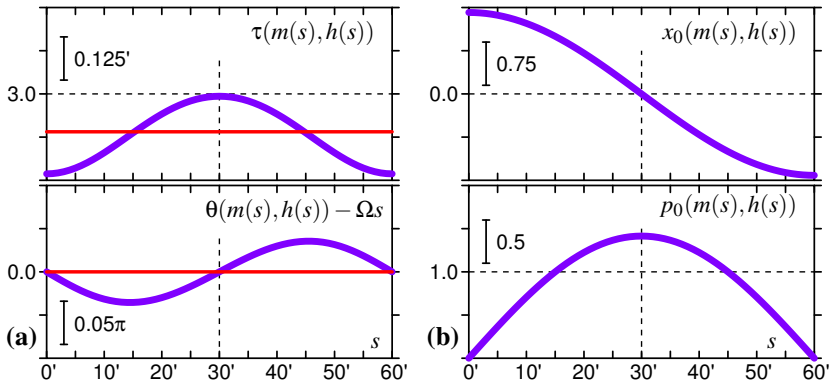

Figure 8: Variation of the period of first return τ (2.51a), the rotation angle θ (2.52a), and the pericentre position given by q_0 and p_0 in (2.35c) along the monodromy circuit Γ (3.1) in fig. 7.

in a sufficiently small neighborhood of a focus-focus equilibrium. Orbits of (2.2) are labeled by the values of SO(2) invariants in sec. 2.2.2. Two principal invariants are needed. If one of them is the Hamiltonian (2.14) itself, then for fixed (m,h), i.e., on a given fibre $\Lambda_{(m,h)}$, the value k of K can be used[16] as a smooth label of SO(2) orbits $\gamma_1 \subset \Lambda_{(m,h)}$. Their homology class is $[\gamma_1]$. Specifically, we can use γ_1 defined in (2.32) and directed by the flow φ_{J_1} in (2.17).

The second cycle $[\gamma_2]$ cannot be defined globally but can be constructed on any particular $\Lambda_{(m,h)}$ in several different ways. The geometric approach of Nekhoroshev is detailed in sec. 4. Here we follow the more "traditional" approach [32, 31] which combines the flows of the Hamiltonian vector fields X_H and X_{J_1} to obtain the periodic flow φ_{J_2} of the vector field X_{J_2} corresponding to the second (local) action J_2. This dynamical construction is a natural continuation of the period lattice method (see sec. 5) going back to [33] and is also a standard way to define J_2 in a sufficiently small open regular neighborhood of $\Lambda_{(m,h)}$.

The closed loops γ_2 are constructed from the reference orbits (2.36) of φ_H which are closed by combining φ_H with the commuting flow φ_{J_1}. The direction on γ_2 corresponds to that of φ_H. First we note that introducing total accumulated rotation angle

$$\Theta = 2\pi\,\mathrm{floor}(s/60), \tag{3.3a}$$

where floor : $\mathbb{R} \to \mathbb{Z}$ returns the closest integer $\mathrm{floor}(g) \le g$, and defining

$$f(s) = h(s) + \mathrm{i}\,m(s), \quad \arg f(s) = \pi - \Omega s \quad \text{and} \quad |f(s)| = \text{const} > 0, \tag{3.3b}$$

with Ω in (3.1) parameterizes solutions (2.36) [as well as general solutions (2.37)] *continuously* for all $(m(s),h(s))$ on Γ in (3.1) and for Ωs extended beyond $[0,2\pi]$ to $\mathbb{R}$. The specific relation (3.3b) between f and Ωs is due to our nonstandard convention for the choice of axes m and h and of the origin for s at the negative-h semiaxis. With these definitions, both x_0 and p_0 in (2.35d) are piecewise smooth (see fig. 8(b)) and positive for $s \in [0,30]$, and each time we cross (see fig. 7) the positive-h semiaxis

[16] Recall that K defines a trivial Morse height function for the $\mathbb{R}^3$ embeddings of $\Lambda_{(m,h)}$, see sec. 2.3.2 and fig. 2, top.

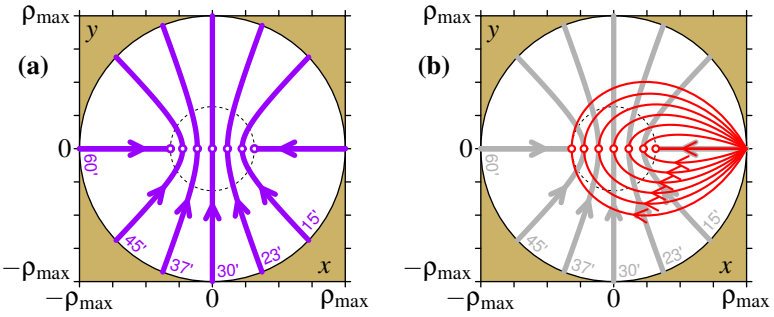

Figure 9: (a) Coordinate space projections of the reference orbits (3.4) of the flow of X_H at various (m,h) corresponding to the points on the monodromy circuit Γ, in fig. 7(b); dashed circle marks the boundary of the inaccessible domain for the initial-final $s = 0'$ and $60'$. (b) Continuous family of closed loops γ_2 in (3.5) which represent the homology class $[\gamma_2]$ of the fibres $\Lambda_{(m,h)}$ and which are obtained by correcting reference orbits by the flow of X_{J_1}. In these plots, $R_{\max} = 1$ and axes x and y are scaled in units of $\rho_{\max} = \sqrt{2}$.

$\{h > 0, m = 0\} \subset \mathsf{R}$, the sign of x_0 changes as the value of x_0 passes through 0, while each time we cross the negative-h semiaxis $\{h < 0, m = 0\} \subset \mathsf{R}$, the same happens to p_0. Finally, using the expression (2.51a) for the first return period $\tau(m,h)$, which is a single-valued smooth function on R and therefore a continuous function on $\Gamma \subset \mathsf{R}$ (fig. 8(a)), we introduce a dimensionless variable ξ along the reference orbits so that (2.36) rewrites as

$$\xi \mapsto \mathbf{u}(\xi) = S_{J_1}^{\phi_0} S_H^{\xi\tau} \mathbf{u}_0, \quad \xi \in [-\tfrac{1}{2}, \tfrac{1}{2}] \tag{3.4}$$

with x_0 and p_0 in $\mathbf{u}_0 = (x_0, 0, 0, p_0)^T$ defined in (2.35c) and (3.3), and ϕ_0 an additional phase defining the longitudinal position of the pericentre (for the original reference orbits it is 0). The continuous set of such orbits with $\phi_0 = 0$ and $s \in [0, 60)$ is shown fig. 9(a).

It can be seen from fig. 5(a) that during the time τ, i.e., as ξ goes from $-\frac{1}{2}$ to $\frac{1}{2}$, the reference orbit advances by angle $\theta(m,h)$ along the wall at $\|\mathbf{q}\| = \rho_{\max}$. So if we want a closed orbit, we must rotate back by $\theta(m,h)\xi$. This gives

$$\gamma_2 : \xi \mapsto \mathbf{u}(\xi) = S_{J_1}^{\phi_0 - \xi(\theta+\Theta)} S_H^{\xi\tau} \mathbf{u}_0 \tag{3.5}$$

Here the multivalued function $\theta(m,h)$ on R is defined continuously on $\Gamma \subset \mathsf{R}$ (cf. fig. 8(a)) by taking the value of $\tan^{-1}$ in (2.52a) continuously in the interval $[0, 2\pi)$ and adding Θ in (3.3) which equals zero on the original interval $[0, 60)$ and steps by 2π every time after we complete a tour on Γ. The resulting continuous series of closed directed loops with $\phi_0 = \Theta = 0$ and $s \in [0, 60)$ is shown fig. 9(b). These loops represent the continuously chosen cycle $[\gamma_2]$ of $\Lambda_{(m(s),h(s))}$.

3.2 Basis cycles of $H_1(\Lambda_f)$

There have been several attempts to relate Hamiltonian monodromy to the singularity theory, complex geometry, and Picard-Lefschetz monodromy. Two approaches can be distinguished. The authors of [42, 67] and, more recently, of [64] show that the integrals defining periods and rotation angles on individual tori are related closely

to Abelian integrals and standard singularities in [8–10]. In the more ambitious programme of [22, 13, 29, 30], monodromy of the fully complexified Hamiltonian system (with complex-valued time, energy and momentum) is considered, and a relation to the real system is attempted. However, in this approach, one should make sure that the path along which complex (m,h) vary is homotopic to the one used in the real system. Due to the topology of the critical value set of the complexified $\mathcal{EM}$-map, this may not always be the case [22].

We continue the more pragmatic approach[17] in sec. 2.4, where relying on an appropriately chosen complex structure in $\mathrm{T}^*\mathbb{R}^2$, we defined an explicit isomorphism (2.25) and identified combined level sets (fibres) $\Lambda_{(m,h)} \subset \mathbb{R}^4$ of real functions (J_1, H) on $\mathbb{R}^4$ and level sets $\Lambda_f \subset \mathbb{C}^2$ of complex-valued function F. This isomorphism of level sets $\Psi|\Lambda$ extends naturally to respective homologies $H_1(\Lambda_{(m,h)}) \to H_1(\Lambda_f)$. Furthermore, by the map (2.28) our monodromy circuit Γ is transferred in the complex domain $\mathbb{C}\setminus 0$ of the regular values f of (2.26) and becomes the path taken in the Picard–Lefschetz theory to describe the monodromy of the $\Lambda_{f,f\neq 0}$ bundle near the A_1 singularity. Then from the Picard–Lefschetz monodromy transformation of $H_1(\Lambda_f)$ we obtain immediately the Hamiltonian monodromy transformation of $H_1(\Lambda_{(m,h)})$. To illustrate this here, we construct explicitly the cycle basis $\{[\gamma_1],[\gamma_2]\}$ of $H_1(\Lambda_{(m,h)})$ and show that under $\Psi|\Lambda$ it becomes a basis of $H_1(\Lambda_f)$.

Applying the linear map Ψ in (2.25) to the loops γ_1 and γ_2 defined in eqs. (2.32) and (3.5) of the previous section, we can now describe the basis $H_1(\Lambda_f)$ using $\Psi(\gamma_1)$ and $\Psi(\gamma_2)$, which we will denote again as γ_1 and γ_2 because it is usually sufficiently clear from the context whether we mean the loops themselves or their images on $\Lambda_f \subset \mathbb{C}^2$ under Ψ. Recall from sec. 2.4 the specific representation of Λ_f used in the Picard–Lefschetz theory, namely a selfintersecting 2-surface S_f immersed in $\mathbb{R}^3$ with coordinates (x, p_y, k) and its projection on the plane $\mathbb{R}^2$ with coordinates (x, p_y).

We obtain the first basis cycle $[\gamma_1]$ of $H_1(\Lambda_f)$ from the $\mathbb{S}^1$ orbits (2.32) of φ_{J_1} in (2.17). In the Picard–Lefschetz theory, $[\gamma_1]$ is called *vanishing cycle*[18]. Because the (x, p_y)-projections of γ_1 with $k<0$ and $k>0$ have opposite directions[19], our definition of γ_1 gives the orientation of S_f described in sec. 2.4 and illustrated in fig. 3(c). A different way to see that explicitly is via a homotopy that takes γ_1 from $k<0$ half of the surface to the $k>0$ half. When regarded in the (x, p_y) projection, this homotopy looks like a reflection of γ_1 in the axis $\{p_y = 0\}$ which necessarily inverts the direction of γ_1. This is illustrated in fig. 10.

The second cycle $[\gamma_2]$ of $H_1(\Lambda_{(m,h)})$ is constructed in sec. 3.1 above using the 2π-periodic flow of the locally constructed Hamiltonian vector field X_{J_2}. The path γ_2 in (3.5) is defined as a path in $\mathbb{R}^4 \supset \Lambda_{(m,h)}$ with positive direction on γ_2 corresponding to increasing K. Reflection at the wall $\|\mathbf{q}\| = \rho_{\max}$ (sec. 2.5) makes $\Lambda_{(m,h)}$ a torus and makes γ_2 a closed fundamental loop on it. Under Ψ in (2.25) the path γ_2 becomes a path in $\mathbb{C}^2 \supset \Lambda_f$, see, for example, the representation of this path on the $s = 0'$ Riemann surface in fig. 10. We should make sure that the resulting first homology cycle $[\Psi(\gamma_2)]$ suits the Picard–Lefschetz theory.

In this theory, $[\gamma_2]$ is a *relative cycle* of non-compact fibres Λ_f called *co-vanishing* cycle. To use our $[\Psi(\gamma_2)]$ in the non-compact case, consider extending γ_2 in (3.5) as $R_{\max} \to \infty$ at given fixed (m,h). Since K is a height function on Λ_f, the path γ_2 that goes

[17] Our construction is essentially contained in the more general setting of [41, 29, 30] where specific restrictions on F and specific complex symplectic form give in our case the same isomorphism.

[18] see, for example, the introduction in [9, 10] where γ_1 is denoted Δ.

[19] Indeed from (2.32) we see that $\dot{x} = -A_- \sin t$ and $\dot{p}_y = A_+ \cos(t+\alpha')$, and in particular $\dot{x}(0) = 0$ and $\dot{p}_y(0) = A_+ \cos\alpha' = 2k$.

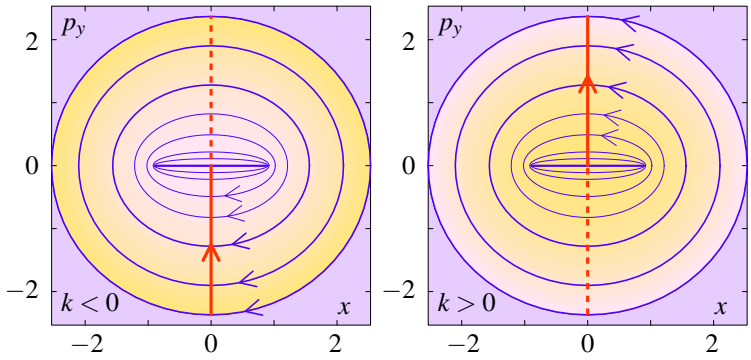

Figure 10: The (x,p_y) projections of the lower ($k<0$) and upper ($k>0$) parts of the embedding S_f of the regular fibre Λ_f with $\operatorname{Im} f=0$ and $\operatorname{Re} f<0$ shown in fig. 3(b) and (c). The $\mathbb{S}^1$ loops represent orbits γ_1 defined in (2.32), the bold vertical line shows the path γ_2 defined by (3.5) with $\phi_0=-\pi/2$, $\Theta=0$ and $s=0'$. The observer is at $k\gg 0$ and the dashed half of γ_2 lies on the invisible part of S_f. Pulling a loop γ_1 from the lower to the upper part or vice versus through the critical section at $k=0$ is a homotopy on S_f which results in changing the direction of the (x,p_y) projection of γ_1. The concrete values of $K_{\max}$ and $|f|$ used for the plot are 3 and 0.4 respectively; the orbits γ_1 are drawn for $|k|=0$, 1, 2, 3, and additionally for $k=0.05$, 0.1, 0.25, 0.5 (finer lines).

from $-K_{\max}$ to $+K_{\max}$ will in this limit give a curve γ_2^* representing a relative cycle of Λ_f. For the purposes of the Picard–Lefschetz theory, we should further require that in comparison to its "central" part γ_2, the full curve γ_2^* does not depend essentially on (m,h) outside sufficiently large γ_2. In this way, the imprint of the singularity Λ_0 in the cycle bases of regular fibres is localized[20]. To verify that γ_2 in (3.5) satisfies these requirements, replace θ in (3.5) for its asymptotic value (2.52b) in the limit $|f|\ll R_{\max}$, use (2.35d) for $\mathbf{u}_0=(x_0,0,0,p_0)^T$ and compute the endpoints of γ_2

$$\begin{aligned}\mathbf{u}_{\xi=\pm\frac12} &= S_{J_1}^{\phi_0\mp(\Theta+\pi-\arg(f))/2} S_H^{\pm\tau/2}\mathbf{u}_0\\ &= \frac{\sqrt{|f|}\,\mathrm{e}^{\tau/2}}{\sqrt{2}} S_{J_1}^{\phi_0\mp\Theta/2}\left(1-\frac{h}{\mathrm{e}^\tau},\mp\frac{m}{\mathrm{e}^\tau},\pm1\pm\frac{h}{\mathrm{e}^\tau},\frac{m}{\mathrm{e}^\tau}\right)^T.\end{aligned}$$

For sufficiently large asymptotic $\tau\approx\log 4R_{\max}$ in (2.51b) and $K_{\max}\approx R_{\max}$ in (2.16), the result is essentially independent on $\arg(f)$, i.e., on the point on the monodromy circuit Γ. So the condition $|f|\ll R_{\max}$ assures the correspondence between our compact Hamiltonian case and the Picard-Lefschetz analysis.

3.3 Hamiltonian monodromy

The first homologies $H_1(\Lambda_{(m,h)})$ with cycle bases $\{[\gamma_1],[\gamma_2]\}$ form a locally trivial bundle over the $\mathbb{S}^1$ circuit Γ in eq. (3.1) and fig. 7. As we follow Γ, the globally defined cycle $[\gamma_1]$ remains unchanged: for any $(m,h)\in\mathsf{R}$ such as $(m(s),h(s))\in\Gamma\in\mathsf{R}$, an orbit γ_1 projects to a circle in the $\mathbf{q}$-plane directed counterclockwise and parallel to the wall. If any proof of this is needed—use (2.32). So in particular

$$\gamma_1(60')=\gamma_1(0')=\gamma_1. \tag{3.6a}$$

[20]The full significance of this requirement of the Picard-Lefschetz theory becomes clear in sec. 3.4.

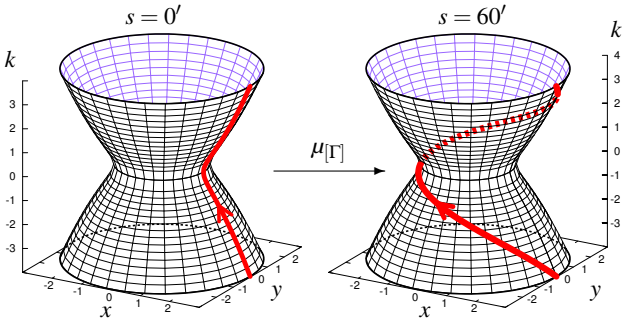

Figure 11: Cycles γ_2 in (3.5) defined for $s = 0'$ and $60'$ which correspond to the initial and final point on the monodromy circuit Γ in (3.1). The initial-final torus $\Lambda_{(m,h)}$ with $(m,h) = (0,-1)$ is shown embedded in $\mathbb{R}^3$ with coordinates (x,y,k) as described in sec. 2.3.2, cf. fig. 2.

On the other hand, the initial cycle $[\gamma_2(0')]$ and the final cycle $[\gamma_2(60')]$ are different. We can easily see this in fig. 9(b) which illustrates (3.5). For $s = 0'$, i.e., for $m = 0$ and $h < 0$, the orbit $\gamma_2(0')$ projects to a radial line in the $\mathbf{q}$-plane, while $\gamma_2(60')$ projects into a loop which has one point on the wall with $\|\mathbf{q}\| = \rho_{\max}$ and which encircles clockwise the classically forbidden region around $\mathbf{q} = 0$. The respective rotation angles $\theta(0')$ and $\theta(60')$ equal 0 and 2π. The three-dimensional representation of the initial-final fibre $\Lambda_{(m=0,h<0)}$ in fig. 11 can further help to understand the situation. This representation clearly shows that $\gamma_2(0')$ and the final cycle $\gamma_2(60')$ are not homotopic to each other.

Comparing to the Picard-Lefschetz theory, it is worth recalling that here we are on a torus where γ_2 is a closed fundamental loop (sec. 2.5). So $[\gamma_2]$ is a cycle of $H_1(\mathbb{T}^2)$ and not a relative cycle of a noncompact fibre. Moreover, transforming $\gamma_2(60')$ homotopically[21] on $\Lambda_{(m=0,h<0)}$ we observe that

$$\gamma_2(60') = \gamma_2(0') - \gamma_1 . \tag{3.6b}$$

Expressing (3.6a) and (3.6b) in the matrix form, we get the statement of theorem 3.1

$$\begin{pmatrix}\gamma_1\\ \gamma_2\end{pmatrix}_{s=60'} = \begin{pmatrix}1 & 0\\ -1 & 1\end{pmatrix}\begin{pmatrix}\gamma_1\\ \gamma_2\end{pmatrix}_{s=0'} . \tag{3.6c}$$

A different convenient way to visualize the continuous evolution of γ_2 relies on replacing the $\mathbb{R}^3$ embeddings of regular fibres $\Lambda_{(m,h)}$ (fig. 11) by their $\mathbb{R}^2/\mathbb{Z}^2$ trivializations which we called q-charts and p-charts (see fig. 2). Even though these trivializations are, obviously, not canonical $\mathbb{T}^2 \to \mathbb{R}^2/\mathbb{Z}^2$ (because neither of their coordinates is a canonical angle), they are locally equivalent to a canonical chart and give a similar representation of what happens[22]. The only problem arises for $m = 0$ when one of these trivializations becomes singular and we are forced to use a particular one trivialization near $m = 0$: a q-chart for $h < 0$ and a p-chart for $h > 0$. Consequently, we will have to switch between the q and p charts in order to complete a tour on Γ. For $m \neq 0$ this can be done using diffeomorphism (2.23b).

Note that the q-chart is easily comparable to fig. 9(b) and 11. In fig. 12, we used the q-chart everywhere except near the "upper point" point $\Gamma_4 = \Gamma \cap \{m = 0, h > 0\}$

[21] The most convenient orbit for that is γ_1 with $k = 0$, i.e., the one giving the boundary of the classically forbidden region in the $\mathbf{q}$-plane.

[22] For an example of using canonical trivializations, see [49].

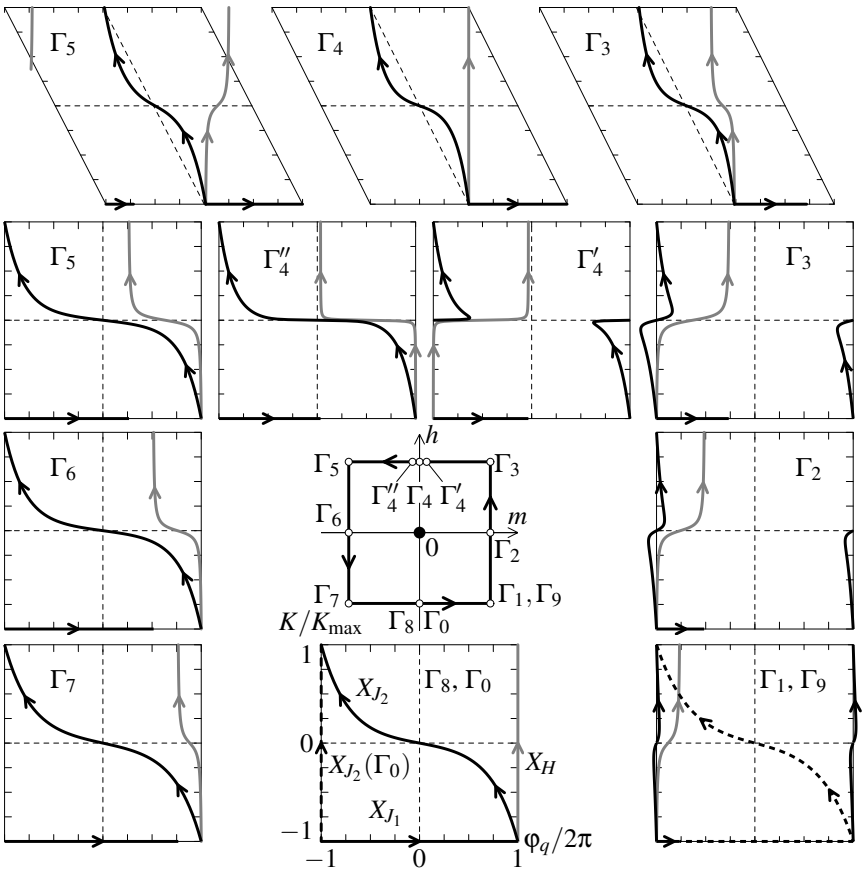

Figure 12: Construction of the continuous family of cycles for the regular fibers $\Lambda_{(m,h)}$ with (m,h) on the circuit Γ (center). Dimensionless coordinates $(\varphi_q, K/K_{\max})$ and $(\varphi_p, K/K_{\max})$ on q-charts and p-charts (top row), respectively, correspond to those in sec. 2.3.2 and fig. 2. Each chart shows the second cycle representative γ_2 (bold line) given by (3.5) and its decomposition using the trajectory of the system with Hamiltonian H in (2.14) (gray line) and part of the orbit of the flow of the system with Hamiltonian J_1 in (2.10a) (bold horizontal line), i.e., the orbit of the axial symmetry action (2.2); arrows correspond to positive time increase. Dashed bold lines on the q-charts for Γ_8 and Γ_1 (bottom center and right) indicate cycles for $\Gamma_0 = \Gamma_8$ and $\Gamma_9 = \Gamma_1$ respectively.

to illustrate the evolution of γ_2. Denoting points that mark characteristic stages of the evolution as Γ_0, Γ_1, etc, which can be easily associated with the values of $s \in [0, 60]$ in fig. 7(b), we begin at the "lower" point $\Gamma_0 = \Gamma \cap \{m = 0, h > 0\}$ with γ_2 going straight along axis K (vertical dashed line denoted $X_{J_2}(\Gamma_0)$ in the bottom center panel of fig. 12). This γ_2 deforms smoothly as we move along counterclockwise through Γ_1, Γ_2, up until Γ_3 and compensate the nonperiodic orbit of the flow of X_H (bold gray) by subtracting an appropriate segment of the orbit of the flow of X_{J_1} shown at the bottom of each panel. At Γ_3, because our q-chart becomes singular later at Γ_4, as can be observed clearly at the nearby points Γ'_4 and Γ''_4, we switch to the p-chart using (2.23b). We continue smoothly to Γ_5 where we switch back to the q-chart and then complete the

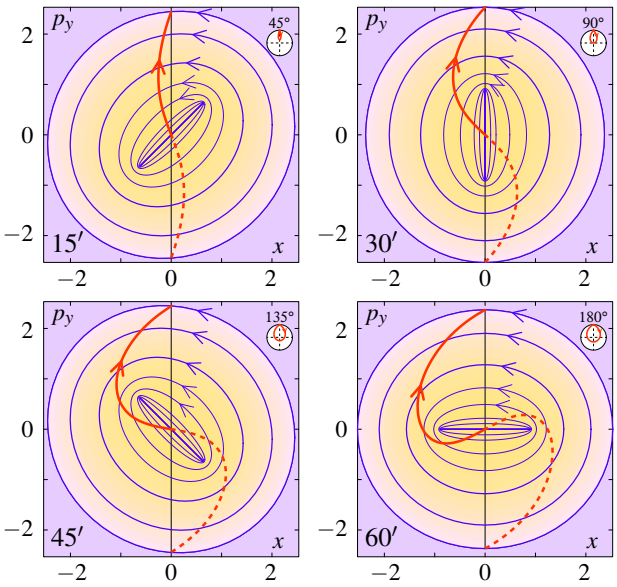

Figure 13: Projections of the upper ($k > 0$) part of the Riemann surfaces S_f (cf. fig. 10) and paths γ_1 (closed loops) and γ_2 (bold line, solid for $k > 0$ and dashed for $k < 0$) representing basis elements of $H_1(\mathsf{S}_f)$ for different $f(s)$ on the monodromy circuit $\psi(\Gamma) \subset \mathbb{C} \setminus 0$. The initial path γ_2 for $s = 0'$ is shown in fig. 10. The value of s is indicated in the lower left corner of each snapshot, $f(s)$ is given by (2.28) and (3.1). The angle by which the branch points have rotated is indicated in the upper right corner. Also shown in this corner is the miniature $\mathbf{q}$-space projection of γ_2, cf. fig. 9(b).

tour returning to $\Gamma_8 = \Gamma_0$ by way of Γ_6 and Γ_7. We read (3.6b) from the $\Gamma_8 = \Gamma_0$ panel of fig. 12.

Equations (3.6) show that the cycle basis $\{[\gamma_1], [\gamma_2]\}$ cannot be chosen globally over Γ and that the system has nontrivial monodromy. As was already mentioned before, the monodromy transformation (3.6) depends neither on the choice of the initial–final point on Γ, nor on the particular circuit Γ within the homotopy class $[\Gamma]$. This signifies that the cycle basis $\{[\gamma_1], [\gamma_2]\}$ cannot be chosen globally for all regular $(m,h) \in \mathsf{R}$ and that $H_1(\Lambda_{(m,h)})$ form a nontrivial bundle over the whole R as well as over the particular Γ in (3.1).

3.4 Picard-Lefschetz monodromy

Due to the isomorphism of the fibres Λ_f and $\Lambda_{(m,h)}$, of their first homologies, and of the paths along which f and (m,h) vary, Hamiltonian monodromy of our compact system is entirely equivalent to the Picard-Lefschetz monodromy characterizing the A_1 singularity. To illustrate this equivalence, which extends naturally to any Hamiltonian system with nondegenerate focus-focus singularity, we compute below the monodromy transformation of $H_1(\Lambda_f)$ in the way it is usually done in complex geometry.

Under the linear map (2.28), our circuit (3.1) becomes an equivalent homotopically nontrivial $\mathbb{S}^1$ path $\psi(\Gamma)$ in the set $\mathbb{C} \setminus 0$ of regular values[23] of F in (2.26). Notice that

[23]The set of regular values of F in (2.26) is larger than that of $\mathcal{EM}$ because there is no wall reflection (sec. 2.5) in the standard Picard-Lefschetz theory and fibres Λ_f are non-compact.

$\psi(\Gamma)$ has negative direction with respect to the standard orientation of $\mathbb{C}$. We analyze the evolution of the Riemann surface S_f of (2.31). As f follows $\psi(\Gamma)$ and completes one tour, the branch points $\pm\sqrt{f}$ go half-way around a circle in $\mathbb{C}$ of radius $\sqrt{|f|}$. This does not affect qualitatively the basis cycle $[\gamma_1]$ which encircles the two branch points points and the interleave line connecting them. We have (3.6a). At the same time, because it crosses the interleave line, the basis cycle $[\gamma_2]$ is deformed in order to evolve continuously with f. Taking our explicit realization of S_f as Λ_f embedded in $\mathbb{R}^3$ (see sec. 2.4), and our concrete γ_1 and γ_2, we can follow this evolution in detail as illustrated in fig. 13.

In order to compare the final path $\gamma_2(60')$ and the initial path $\gamma_2(0')$ drawn in the last snapshot of fig. 13 and in fig. 10, respectively, consider their difference[24]

$$\delta_{\gamma_2} = \delta_- \cup \delta_+ = \gamma_2(60') - \gamma_2(0'), \tag{3.7}$$

where δ_+ and δ_- lie in the respective $k>0$ or $k<0$ halves of the Riemann surface S_f with $f = s(0') = f(60') = h < 0$ as depicted in fig. 14(a). Deforming δ_{γ_2} homotopically on S_f, we show that it is equivalent to $-\gamma_1$.

First we deform both δ_- and δ_+ keeping their two intersection points on the $k=0$ interleave line fixed. The deformation of δ_- is illustrated in fig. 14(b) and 14(c), that of δ_+ (dashed line in fig. 14) is entirely similar. We recall that $\gamma_2(60')$ and $\gamma_2(0')$ are defined so in sec. 3.2 that for large $|k| \gg |f|$ they approach each other asymptotically, and in the compact case with explicit $K_{\max}$ cutoff of S_f, they connect at points with $k = \pm K_{\max}$. This means that the $|k| \gg |f|$ part of δ_{γ_2} is homotopic to zero and can be removed. So we obtain a closed path $\tilde{\delta}_{\gamma_2} = \tilde{\delta}_- \cup \tilde{\delta}_+$ in the neighbourhood of $k=0$, see fig. 14(d). Each half of $\tilde{\delta}$ is a semicircle going along $-\gamma_1$ and connected to $k=0$ by segments of two different representatives of $[\gamma_2(0')]$. Notice once more that this deformation—and therefore all that follows it—is only possible due to the fact that at large $|k|$ our cycle bases are essentially insensitive to the changes in f.

The next step is "pulling" one of $\tilde{\delta}_\pm$ through the $k=0$ interleave line. Recall from sec. 2.4 and 3.2 that the direction of the (x, p_u) projections of the closed paths γ_1 changes when these paths are moved across the interleave line. Similar thing happens to $\tilde{\delta}_\pm$. So moving $\tilde{\delta}_+$ homotopically from the $k>0$ part of S_f to the $k<0$ part results in fig. 14(e). Now it becomes obvious that the two $k=0$ points of δ_{γ_2} which remained fixed throughout all these deformations belong to "appendices" that are homotopic to 0. Removing the latter we arrive at $-\gamma_1$ in fig. 14(d) and we obtain (3.6b) which corresponds to the Picard-Lefschetz formula

$$\delta_{\gamma_2} = (-)^\Gamma \operatorname{ind}(\gamma_1 \cap \gamma_2)\, \gamma_1 \tag{3.8}$$

where $(-)^\Gamma$ equals $+1$ or -1 depending on whether the circuit Γ is directed counterclockwise or clockwise with respect to the orientation of the complex line $\mathbb{C}$ of the values of (2.26), and $\operatorname{ind}(\gamma_1 \cap \gamma_2)$ is the intersection index of γ_1 and γ_2 with respect to the orientation of the constant level set Λ_f defined by the complex structure on the Riemann surface of (2.31). In our case $(-)^\Gamma = -1$ and $\operatorname{ind}(\gamma_1 \cap \gamma_2) = 1$. The computation of the latter is illustrated in fig. 15, where we can see that at their intersection, the paths γ_1 and γ_2 always define a pair of tangent unit vectors $(\mathbf{e}_1, \mathbf{e}_2)$ which agree with the basis $(\mathbf{e}_{p_y}, \mathbf{e}_x)$ that sets the orientation of Λ_f. Notice that because of this agreement, our orientation of $\Lambda_{(m,h)}$ in the Hamiltonian case (sec. 2.3.2 and sec. 3.1) coincides with that of Λ_f.

[24] Not to confuse with δ in [9] which corresponds to our γ_2; what we denote δ is the variation of γ_2.

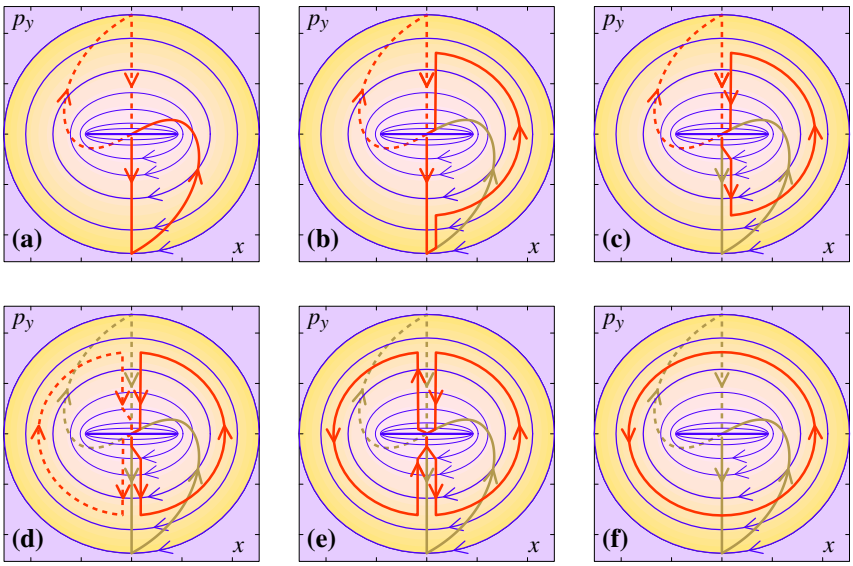

Figure 14: Homotopy of δ_{γ_2} in (3.7) on the Riemann surface S_f (cf. figs. 3, 10 and 13). (a) δ_{γ_2} viewed from the projected lower ($k<0$) part of S_f; the bold solid line shows the visible $k<0$ part δ_- while the dashed line marks the invisible $k>0$ part δ_+; (b) the homotopic transformation of δ_- using half of the path $-\gamma_1$; (c) same as (b) but with the large-$|k|$ part of the deformed cycle removed, so that the result shown by the bold solid line can now be moved homotopically across the $k=0$ interleave line in the centre. (d) δ_+ is transformed similarly to (b)–(c); (e) the deformed δ_+ is brought down to the $k<0$ part, gets flipped in the process with respect to the $\{p_y=0\}$ axis, and becomes visible; (f) after removing parts homotopic to 0, the result is $-\gamma_1$ on the lower part of S_f.

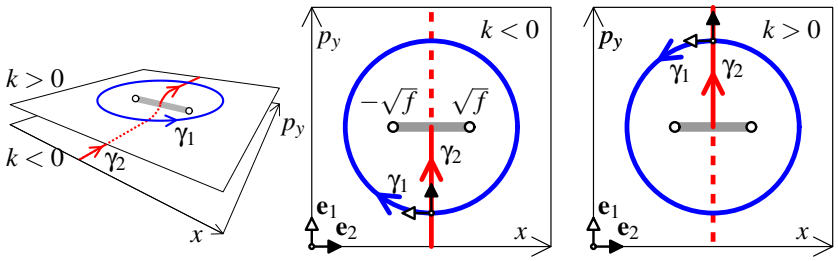

Figure 15: Computing intersection index $\mathrm{ind}(\gamma_1\cap\gamma_2)=1$ on the regular fibre Λ_f with $f=h<0$ represented as a Riemann surface of (2.31) and oriented according to the standard complex structure of $\mathbb{R}^2\sim\mathbb{C}$ with coordinate u in (2.25) and corresponding reference basis $(\mathbf{e}_1,\mathbf{e}_2)$.

3.5 Direction of basis cycles and the "sign" of monodromy

Both Hamiltonian and Picard-Lefschetz monodromy are purely topological phenomena which involve *orientable* regular fibers, tori $\Lambda_{(m,h)}$ and complex curves Λ_f, respec-

tively. Orientability of regular fibres results in the specific feature of these phenomena which we may call their "sign" following the original terminology by Zhilinskií [74].

Remark 3.3. The "sign" of monodromy should not be understood literally as the sign in expressions (3.6b) and (3.8), but rather as a reference to a particular class of $\mathrm{SL}(2,\mathbb{Z})$, cf. [56, 57, 74, 27]. Note that matrices (3.2) are not conjugated in $\mathrm{SL}(2,\mathbb{Z})$ (they belong to different classes of conjugated elements). Also note that $M_- = M_+^{-1}$, i.e., the inverse of M_+, which corresponds to $-\Gamma$ (clockwise), is not in the same class as M_+ itself. Our computations in sec. 3.3 and 3.4 and later in sec. 4 prove that, with all conventions respected, monodromy in the simplest case of a non-degenerated focus-focus equilibrium of an integrable Hamiltonian system with two degrees of freedom is always given by a matrix conjugated to M_+.

Remark 3.4. It can be conjectured [74] that in systems with $n > 2$ degrees of freedom, only matrices of certain classes of $\mathrm{SL}(n,\mathbb{Z})$ should be expected.

Orientation of regular fibres corresponds to the choice of directions of γ_1 and γ_2 and to their resulting intersection index $\mathrm{ind}(\gamma_1 \cap \gamma_2)$. Once these directions are chosen so that all conventions are respected, the monodromy transformation of respective cycles $[\gamma_1]$ and $[\gamma_2]$ is unambiguous.

In the Hamiltonian case [74, 27], the choice of directions of γ_1 and γ_2 coincides with the orientation defined on all fibres in an open neighbourhood $\Sigma_{(m,h)} \subset \mathrm{T}^*\mathbb{R}^2$ of a given regular fibre $\Lambda_{(m,h)}$ by Hamiltonian vector fields (X_{J_1}, X_H). With this orientation, $\mathrm{ind}(\gamma_1 \cap \gamma_2) \equiv 1$. Specifically, γ_1 is naturally directed by X_{J_1}, while the direction vector $\mathbf{e}_2$ of γ_2 is chosen so that $\mathbf{e}_2 \cdot X_H(\mathbf{u}) > 0$ at any point $\mathbf{u} \in \gamma_2 \subset \mathrm{T}^*\mathbb{R}^2$. A slightly different approach that involves a specific height function on $\Lambda_{(m,h)}$ which has a particular γ_2 as its 0-level set is described in sec. 5 of [49] and is used in sec. 4. So it follows that in the Hamiltonian case, the sign in (3.6) is fixed.

In the Picard–Lefschetz theory, directions of γ_1 and γ_2 (and consequently the orientation of Λ_f) are defined with respect to the standard complex orientation of the Riemann surface S_f of (2.31), cf. fig. 15. Given these directions on γ_1 and γ_2 and on the circuit Γ, the variation of the co-vanishing cycle γ_2 is prescribed by the formula (3.8). If the directions agree with the orientation of S_f, the index $\mathrm{ind}(\gamma_1 \cap \gamma_2) = 1$, and we have the same transformation as in the Hamiltonian case.

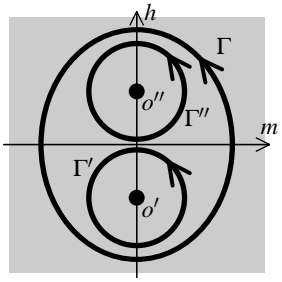

Figure 16: Decomposition of a degenerated isolated singularity into two elementary singularities represented by critical values o' and o'' in the base of the integrable fibration. Circuits Γ' and Γ'' encircle o' and o'', respectively, while $\Gamma = \Gamma' + \Gamma''$ goes around both o' and o''.

Of course, directions of γ_1 and γ_2 may be set externally, irrespectively to the chosen orientation of the fibres. The Picard-Lefschetz formula takes care of all such trivial changes. The "sign" property can be best understood when we consider a combination

of two isolated singularities that can be deformed into one single degenerate singularity [14] (several concrete physical examples can be found in [38, 39, 37]). Because of this property, monodromy of the degenerated singularity cannot be trivial. Specifically, let isolated critical values o' and o'' of the *same* integrable map represent two isolated singular fibres (pinched tori or A_1 singularities, depending on the setup) in the base of the integrable fibration (see fig. 16). Then the fundamental group of the base is generated by circuits Γ' and Γ'' encircling o' and o'' respectively. What is the monodromy transformation $\mu_{[\Gamma]}$ corresponding to $[\Gamma] = [\Gamma'] + [\Gamma'']$, and—by deformation—to the combined degenerated singularity? Because monodromy is a homomorphism, we have $\mu_{[\Gamma]} = \mu_{[\Gamma']} \circ \mu_{[\Gamma'']}$, which for monodromy matrices (in some fixed cycle basis) means $M = M'M''$. Because of the sign property, there is no common fixed cycle basis in which $M' = M_+$ and $M'' = M_-$ so that $M = 1$ and $\mu_{[\Gamma]}$ is trivial. As suggested in [24, Proposition 1.8, Remark 1.10], this may no longer hold in the non-Hamiltonian case.

Remark 3.5 (addition of singularities). If a system possesses $k > 1$ nondegenerate focus-focus equilibria $i = 1, 2, \ldots, k$, their monodromy matrices are in the class $[M_+]$, but there may not be a common basis to represent all matrices as matrices in $[M_+]$. The latter can only happen if the system has a semi-global $\mathbb{S}^1$ action and corresponding momentum. If we compute monodromy for a contour Γ which encircles all respective isolated critical values, the monodromy matrix is $M = \Pi_{i=1}^{k} A_i M_+ A_i^{-1}$ with $A_i \in \mathrm{SL}(2, \mathbb{Z})$. For the global $\mathbb{S}^1$ action, we have $M = M_+^k = M_{+k}$ as in the case of a k-pinched torus.

4 Explicit construction of the first homology (H_1) bundle over Γ using a fixed global section (Nekhoroshev)

In this section, we like to emphasize further the topological origins of monodromy. So far, our construction of the cycle $[\gamma_2]$ in sec. 3.1 relied substantially on the detailed study (sec. 2) of the dynamics of the system with Hamiltonian (2.1). At the same time, the correspondence to the Picard-Lefschetz theory, which is uncovered in sec. 3.4, suggests strongly that Hamiltonian monodromy is a basic topological phenomenon of a more general nature. This aspect of monodromy can be seen most clearly in the H_1 bundle construction by Nekhoroshev which he and his colleagues implemented in [48, 49, 53]. In this method, the second cycle γ_2 of H_1 is defined by studying intersections of fibres $\Lambda_{m,h}$ with an appropriately chosen fixed hyperplane $\sigma \in \mathbb{R}^4$. The use of the dynamics on $\mathbb{R}^4$ is reduced to a bare minimum: the dynamics is used to define the directions of the cycles. Specifically, the directions of $[\gamma_1]$ and $[\gamma_2]$ are chosen to agree with that of the flow of the Hamiltonian vector fields, the periodic flow of X_{J_1} and the nonperiodic flow of X_H, respectively. Such fixing directions in accordance with the flows of these Hamiltonian vector fields defines the *sign of monodromy*, cf. sec. 3.5.

It is clear that in order to define γ_2 from intersections $\lambda_{m,h} := \Lambda_{m,h} \cap \sigma$, the hyperplane σ should be transversal to the orbits γ_1 of the flow of X_{J_1}. We can use

$$\sigma := \{y = 0\} \tag{4.1}$$

with coordinate functions (x, p_x, p_y). This plane is transversal to γ_1 when $m \neq 0$. When $m = 0$, we should stay away from the 2-plane $\{x = 0\} \subset \sigma$.

From (2.1a) and (2.10a) we can see that in σ, the intersection $\lambda_{m,h}$ is given by

$$\{x p_y = m, \;\; p_x^2 + p_y^2 - x^2 = 2h\}$$

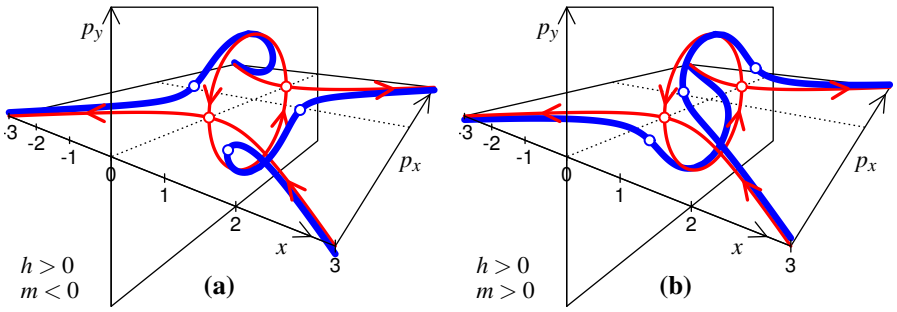

Figure 17: Intersections $\lambda_{m,h}$: regular intersections for $m < 0$ (a) and $m > 0$ (b) consist of two components which are shown by bold lines; the critical intersection for $m = 0$ and $h > 0$, or the "skeleton curve" is shown in both plots by a fine solid line. Direction of the skeleton curves in the planes $\{p_y = 0\}$ and $\{x = 0\}$ is defined by the flow of X_H and X_{J_1}, respectively. Plots are made for $h = 1$ and $|m| = 2/10$.

and we obtain

$$x^2 = \tfrac{1}{2}p_x^2 - h + \sqrt{\left(\tfrac{1}{2}p_x^2 - h\right)^2 + m^2}.$$

It follows that for all $(m,h) \notin \{m = 0, h \geq 0\}$, the intersection $\lambda_{m,h}$ consists of two disconnected components with $x < 0$ and $x > 0$ which do not reach the $\{x = 0\} \subset \sigma$ plane, see fig. 17. The $\lambda_{m=0,h>0}$ is the only *critical* intersection which Nekhoroshev et al. [49] call a "skeleton curve" because as $h > 0$ and m goes to 0, the two components of the regular intersection approach this skeleton in two different incompatible ways corresponding to the limits $m \to 0_-$ and $m \to 0_+$ (left and right in fig. 17). The skeleton curve is a union

$$\lambda_{m=0,h>0} = \{x = 0,\ p_x^2 + p_y^2 = 2h\} \cup \{p_y = 0,\ p_x = \pm\sqrt{2h + x^2}\} \subset \sigma$$

of the circular orbit γ_1 in the $\{x = y = 0\}$ plane and the two hyperbola in the $\{p_y = y = 0\}$ plane, respectively, which intersect in two points

$$o_\pm := \{x = p_y = 0, p_x = \pm\sqrt{2h}\} \in \sigma. \tag{4.2}$$

The direction on the skeleton curve γ_1 is given by the vector field X_{J_1} for $x = y = 0$. In coordinates (x, p_x, p_y) on σ this gives $(0, -p_y, p_x)^T$. The direction of the two other skeleton curves can be defined similarly using X_H for $y = p_y = 0$ which gives vector $(p_x, x, 0)^T$. These directions are indicated in fig. 17 by arrows. They can be used to orient the components of the nearby regular intersection.

Everywhere except when $m \to 0$ for $h > 0$, we will construct the curve γ_2 representing the second basis cycle $[\gamma_2]$ using the positive-x component of $\lambda_{m,h}$. When $m \to 0$ and $h > 0$, we cannot do that because, as can be seen from fig. 17, such component cannot be continued through the critical intersection $\lambda_{m=0,h>0}$. So before we reach $m = 0$ at some fixed $h > 0$, we will "disassemble" our curve γ_2 and we will "reassemble" it back shortly after crossing $m = 0$. The disassembled curve is homotopically equivalent to γ_2 in $\Lambda_{m,h}$ but it does not lie in σ and it does not come close to the $\{x = y = 0\}$ plane and therefore can be continued through $m = 0$, $h > 0$.

We start on Γ like in sec. 3.1, with $m = 0$ and $h < 0$, and continue γ_2 counterclockwise as the $x > 0$ component of $\lambda_{m,h}$. Approaching $m \to 0_+$ we disassemble γ_2

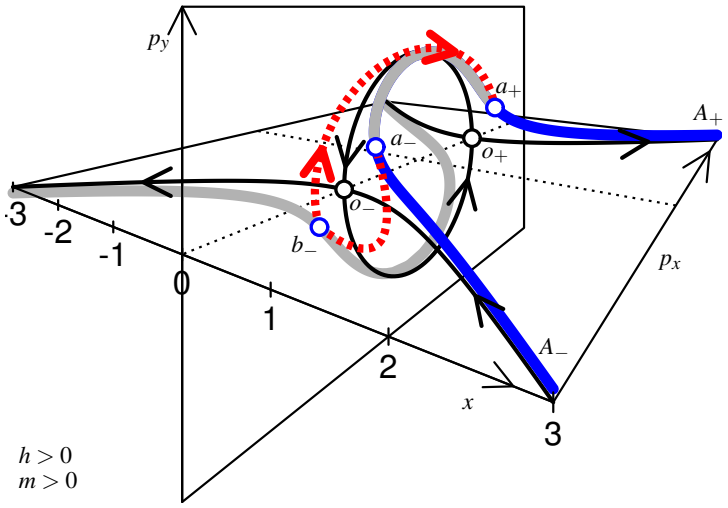

Figure 18: Disassembled $x > 0$ component of the regular intersection $\lambda_{m,h}$ with $m \to 0_+$ and $h > 0$ (bold solid and dashed lines). The unused parts of $\lambda_{m,h}$ are shown in gray. Dashes indicate paths outside σ, notably the small connection δ and part of $-\gamma_1$.

using parts of the $x > 0$ component of $\lambda_{m,h}$ with sufficiently large x, part of γ_1 and a small segment $\delta \not\subset \sigma$. The smallness of the latter assures homotopy. The result is shown in fig. 18. In this figure, we mark points $A_\pm$ and $a_\pm$ on the $x > 0$ component of $\lambda = \lambda_{m>0,h>0}$ and point b_- on the $x < 0$ component of λ. We replace the part $a_-a_+ \subset \lambda$ by the union of $\delta = a_-b_-$ and $b_-a_+ \subset -\gamma_1$. Notice that the connecting path δ is necessary because of the specific way the $\mathbb{S}^1$ orbits γ_1 intersect $\lambda \subset \sigma$, and that the direction on b_-a_+ is *opposite* to that of γ_1. The smallness of δ is guaranteed by the fact that for $m \to 0$ points b_- and a_- remain close to o_-. It follows that the curves

$$\tilde\gamma_2 = A_-a_- \cup \delta \cup b_-a_+ \cup a_+A_+ \quad \text{and} \quad \gamma_2 = A_-a_- \cup a_-a_- + \cup a_+A_+ \subset \lambda$$

are homotopic and we can now continue $\tilde\gamma_2$ to negative m, see fig. 19(a).

We can now "reassemble" $\tilde\gamma_2$ in fig. 19, top in order to eliminate $\delta = a_-b_-$ and use a_-a_+. This involves another piece a_+b_- of $-\gamma_1$ that goes back from a_+ to b_-. Specifically, we can see that $a_-a_+ \cup a_+b_- \cup -\delta$ is homotopic (in $\Lambda_{m,h}$) to a point. We have

$$A_-a_- \cup \delta \cup b_-a_+ \cup a_+A_+ \sim A_-a_- \cup (a_-a_+ \cup a_+b_- \cup -\delta) \cup \delta \cup b_-a_+ \cup a_+A_+,$$

see fig. 19(b). Therefore, our $\tilde\gamma_2$ for $m < 0$ is homotopic to $A_-a_-a_+A_+ \cup -\gamma_1$, i.e., the sum of the $x > 0$ component of $\lambda_{m<0,h>0}$ and $-\gamma_1$. This sum continues along Γ with $m < 0$. Returning to the departure values $m = 0$ and $h < 0$, the curve $A_-a_-a_+A_+$ becomes the original $\gamma_2(0)$. The final $\gamma_2(1)$ is therefore the sum of the original $\gamma_2(0)$ and $-\gamma_1$. The latter was acquired at the crossing of $m = 0$ for $h > 0$ and does not change as we follow Γ, i.e., $\gamma_1(0) = \gamma_1(1)$. So for the respective basis element in H_1 we have

$$[\gamma_2](1) = [\gamma_2](0) - [\gamma_1]$$

and obtain theorem 3.1. The sign in this sum (cf. sec. 3.5) is determined by our choice for the direction on γ_2 to agree with that given by X_H.

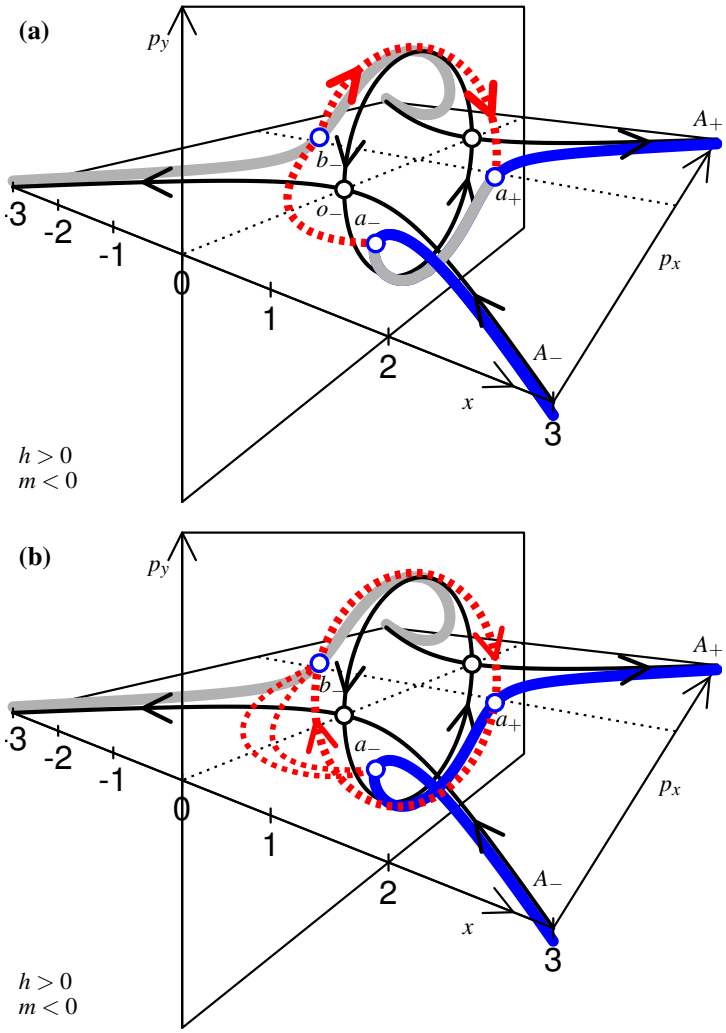

Figure 19: Disassembled (a) and reassembled (b) $x > 0$ component of the regular intersection $\lambda_{m<0,h>0}$ (bold solid and dashed lines). Dashes indicate paths outside σ, notably the small connections $\pm\delta$ and parts of $-\gamma_1$. Curve (a) is a continuation of the one in fig. 18 to negative m; curves (a) and (b) are homotopic.

Remark 4.1. Since the calculation does not involve the analysis of the wall reflection at $\rho_{\max}$, the above method applies to any focus-focus equilibrium. Furthermore, since the very presence of the wall is not important, this method can be used directly to compute "scattering monodromy" of [30, 34] and the Picard-Lefschetz monodromy in sec. 3.4.

5 Discussion

Unlike some other computations of Hamiltonian monodromy, the Nekhoroshev's proof in sec. 4 relies essentially only on the geometry of the fibration of $\mathrm{T}^*\mathbb{R}^2$ into common (m,h)-level sets Λ of J_1 (2.10a) and H (2.1). Hamiltonian dynamics is engaged only in order to remove the ambiguity in the choice of directions for the basis cycles in $H_1(\Lambda)$. Consequently, we have a direct analog of the Picard-Lefschetz computation (sec. 3.4). Minimal and concise, both proofs show that monodromy is indeed a very basic topological phenomenon. At this point, it may be worth to rethink the distinction often drawn in the literature between the so-called "geometric monodromy theorem" [56, 24], and all other studied cases of Hamiltonian monodromy. Instead of exaggerating the specifics of concrete examples, a proper such distinction should, in our opinion, focus on the method employed. From this perspective, Nekhoroshev's method is the most geometric. As for the particularity of concrete systems, such as ours, they can often be shown related directly—if not equivalent to the most general case (sec. 2.8).

The same remark applies to fractional monodromy whose geometric proof was given by Nekhoroshev et al. [49] initially for a concrete example and was developed and generalized later by Nekhoroshev in [54, 53] and eventually in [55] where he improved substantially the original method of [49]. Subsequent treatments [66, 17] which are called explicitly geometric may certainly be more concise and elegant, but are nevertheless a continuation in the direction already set by Nekhoroshev.

As the participant in the original work on fractional monodromy, the author of these notes is well positioned to tell the story of its discovery. Our long discussions initiated when Nikolaí Nekhoroshev began his visit as invited professor in Dunkerque in autumn 2001. He suggested a class of model systems, the $1{:}(-k)$ resonant oscillators with compactifying smooth high order terms, while Boris Zhilinskií proposed "fractional monodromy" as a natural possible formal defect of integer (quantum) lattices [74, 60]. When Boris left for several months in the spring of 2002 and Nikolaí moved to Boulogne-sur-Mer, we faced together the difficult task to work out the relation of Boris' conjecture to classical mechanics. At the beginning, Nekhoroshev was cathegorical that monodromy could not be "fractional" (and it is not, since it is a transformation of basis cycles in H_1 and so is given by a matrix over $\mathbb{Z}$). It took the concrete example of the quantized $1{:}(-2)$ resonance system [48] and its interpretation to direct him towards his understanding of what went on. The three of us were able to finalize the proofs later, after many sessions of difficult work and meetings that continued, with interruptions, over several years until his stay in Milan in 2005. For a long time, Nikolaí remained suspicious of the "sign" of Hamiltonian monodromy (sec. 3.5) which he finally accepted after detailed scrutiny of the H_1 bundle construction in our final proof [49]. Indeed, as we have seen in sec. 3, accounting for this property makes any proof much longer. Nikolaí worked only in Russian. Very sharp and attentive to details, and at the same time, reaching far ahead and widely to other domains that he understood and felt so profoundly, he could iterate painstakingly over and over the same paragraph, lemma, or definition. Sometimes, the result of the whole day spent together amounted to a half-page, and sometimes it was—frustratingly—rejected the next day. Nekhoroshev became clearly convinced of the originality of our discovery and produced several mathematical sequel papers on the subject [55, 54, 53]. Knowing how diligently he worked, and how carefully and economically he was choosing his statements, we, as his readers, have now a difficult responsibility of understanding these works fully. Nikolaí admitted the necessity of solid complete proofs, but most of all, he aimed at conceptual cleanless and universality. He used to say: *Let us make sure that this is right! As for the (elegant) proofs—others will follow and come up with them*. And they did, fortunately.

Beyond the basic case which we consider in the present article, the correspondence of isolated singularities in Hamiltonian systems and those in complex geometry

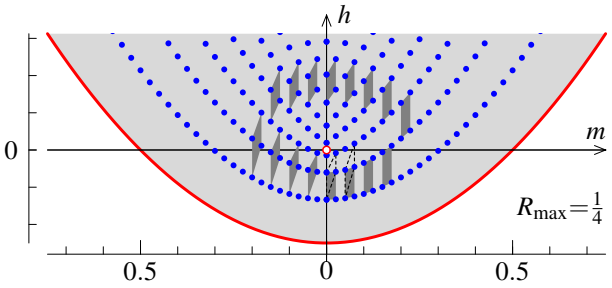

Figure 20: Image of the $\mathcal{EM}$ map of the hyperbolic billiard with $R_{\max} = 1/4$, cf. fig. 1 and 7(a), and the lattice of joint energy-momentum eigenvalues (black dots) of the corresponding quantum system with $\hbar = 1/40$ according to [61]. Dark shaded quadrangles illustrate the evolution of a quantum elementary cell (Zhilinskií's lattice defect diagram). Quantum monodromy defines the relation of initial and final cells.

[9, 44] is difficult to examine fully. To our knowledge, no reciprocal analogies, at the level of detail similar to the one in our study, have yet been suggested for fractional Hamiltonian monodromy [48, 49, 54, 53, 55], or for singularities in [9, chap. II.16] other than A_1. The problem seems to be related to the compactness of the fibres in the Hamiltonian case and the resulting global properties of Hamiltonian monodromy. So in Hamiltonian dynamical systems, two major additional possibilities can be distinguished for a basis cycle of the first homology group of the regular fibres: (i) it can connect the neighbourhoods of several different singular points or (ii) it can re-enter several times the neighbourhood of the same singular point. These cases correspond to degenerate singularities and to fractional monodromy, respectively. Degenerate singularities, known as k-pinched tori, can be deformed into a system of A_1-type points (sec. 3.5). On the other hand, complex geometry of fractional monodromy, such as near the $1{:}(-2)$ oscillatory singular point [48, 49], can be, possibly, uncovered using its branched covering [35] that removes (uncurls) "weak" singularities and turns the system back to the basic A_1 type. In both situations, reduction of naturally pertinent descrete symmetries can provide further insight. At the other end, with regard to complex curves, their suitable compactification becomes more complicated in comparison to the basic case A_1. For example (cf. [42]), one can attempt treating A_3 similarly to A_1, while A_2 and A_4 require clearly a different approach. Further understanding can be gained from deforming higher types into several basic A_1 singularities [43, 44].

Our concrete system, despite its seeming simplicity and specific properties, allowed deep understanding and illustration of several most general aspects of the theory. As detailed in [61], we can naturally extend this study to other topics, always taking advantage of computing everything explicitly. Computation in sec. 2.7.7 of the rotation angle $\theta(m,h)$ and period $\tau(m,h)$ given by integrals (2.49) and (2.50) is the basis of Hamiltonian methods of describing monodromy, often referred to as period lattice computation [28, 20, 21, 36]. One such method is detailed in sec. 3.3. Explicit computation of such integrals can be difficult in a general case and is, in fact, unnecessary, since all we need to know is the variation $\delta\tau(m,h)$ and $\delta\theta(m,h)$ over the circuit Γ. Complexifying the integrals and turning to the cohomology on the regular fibers over Γ results in the study of Gauss–Manin connections [45]. The related theory of Abelian integrals can be used to compute Hamiltonian monodromy in sec. 3.3 as Gauss–Manin monodromy [40]. Doing this for our example system [61] shows, however, that the computation is longer than one may expect when the sign (sec. 3.5) has to be accounted for. Naturally, similar

techniques can be applied to the action integrals themselves, cf. [71, 40]. In fact, given that (2.10a) is a globally defined action, what we need is a pull back $\mathcal{J}_2(m,h)$ of the (locally defined) second action J_2 by the energy-momentum map $\mathcal{EM}$. In our case this function has a simple form [61]

$$2\pi\,\mathcal{J}_2(m,h) = -m\,\theta(m,h) + h\,\tau(m,h) + |f|\sinh(\tau(m,h)) \tag{5.1a}$$

$$\approx m\arg(f) - h\log(|f|) - m\pi + h\,(1+\log 4R_{\max}) + \ldots \tag{5.1b}$$

The asymptotic form (5.1b) with $0 < |f| \ll R_{\max}$ is what one expects generally (cf. remark 2.14) near the focus-focus singularity. Its first term $m\arg(f)$ reflects the log-multivaluedness of $\mathcal{J}_2$ [69] and is at the root of monodromy. These expressions provide the most direct access to the study of the domain that represents the system (the base of the fibration $\bar{\mathsf{R}}$) in the action space [65, 70] and most importantly, of the integer lattice (affine integral structure) [74, 49] in $\bar{\mathsf{R}}$. The latter corresponds to the joint energy-momentum spectrum of the quantum analog system. Quantum monodromy [23, 68, 59, 25, 26, 49] is observed in this latice as a point defect [23, 74]. To present this perspective more definitely, we like to include fig. 20 showing the quantum spectrum of our system. Quantum monodromy is given in this figure by the transformation of the basis cell of the lattice after the cell is taken on its tour on $\Gamma \subset \mathsf{R}$ around $(0,0)$.

Acknowledgments

The author benefited in 2007–2008 from the support by the University of Groningen and the NWO mathematics cluster NDNS$^+$. Many thanks go to Konstantinos Efstathiou for our discussions on the relation between the Hamiltonian monodromy and the A_1 singularity held during the author's visit to Groningen in 2007. We also thank Boris Zhilinskií and Henk Broer for many helpful discussions and encouragements.

References

[1] A. M. Abramov, Vl. I. Arnol'd, A. V. Bolsinov, A. N. Varchenko, L. Galgani, Boris I. Zhilinskií, Yu. S. Iliyashenko, V. V. Kozlov, A. I. Neistadt, V. I. Piterbarg, A. G. Khovanskií, and V. V. Yaschenko. Nikolaí Nikolaevich Nekhoroshev (obituary). *Uspekhi Mat. Nauk*, 64(3/387):174–178, 2009. URL http://mi.mathnet.ru/umn9288. In Russian.

[2] J. M. Arms. Symmetry and solution set singularities in Hamiltonian field-theories. *Act. Phys. Pol. B*, 17:499–523, 1986.

[3] J. M. Arms. Reduction of Hamiltonian systems for singular values of momentum. *Contemp. Math.*, 81:99–110, 1988.

[4] J. M. Arms, M. J. Gotay, and G. Jennings. Geometric and algebraic reduction for singular momentum maps. *Adv. Math.*, 79:43–103, 1990.

[5] J. M. Arms, R. H. Cushman, and M. J. Gotay. A universal reduction procedure for Hamiltonian group actions. In T. Ratiu, editor, *Geometry of Hamiltonian systems*, pages 33–51. Springer Verlag, New York, 1991.

[6] Vl. I. Arnol'd. *Mathematical methods of classical mechanics*, volume 60 of *Graduated Texts in Mathematics*. Springer-Verlag, New York, 2 edition, 1989. Translated by K. Vogtmann and A. Weinstein.

[7] Vl. I. Arnol'd. *Arnold's problems*. Springer-Verlag, Berlin, 2004. Translated and revised edition of the 2000 Russian original; PHASIS, Moscow, 2004. xvi+639 pp.

[8] Vl. I. Arnol'd, A. N. Varchenko, and S. M. Gusein-Zade. *Osobennosti differentsiruemykh otobrazhenií. Klassifikatsiya kriticheskikh tochek, kaustik i volnovykh frontov*. Nauka, Moscow, 1982. in Russian, English title: Singularities of differentiable maps. Classification of critical points, caustics, and wave fronts.

[9] Vl. I. Arnol'd, A. N. Varchenko, and S. M. Gusein-Zade. *Singularities of differentiable maps. Monodromy and asymptotics of integrals*. Nauka, Moscow, 1984. in Russian, see English translation [10].

[10] Vl. I. Arnol'd, S. M. Gusein-Zade, and A. N. Varchenko. *Singularities of differentiable maps. Vol. II. Monodromy and asymptotics of integrals*, volume 83 of *Monographs in Mathematics*. Birkhäuser, Boston, Mass., 1988. Translated from Russian by Hugh Porteous. Translation revised by the authors and James Montaldi. viii+492 pp.

[11] Vl. I. Arnol'd, V. V. Kozlov, and A. I. Neíshtadt. *Mathematical Aspects of Classical and Celestial Mechanics. Dynamical Systems III*, volume 3 of *Encyclopedia of Mathematical Sciences*. Springer-Verlag, Berlin, 1988.

[12] Vl. I. Arnol'd, V. A. Vassil'ev, V. V. Goryunov, and O. V. Lyashko. *Singularities. Local and global theory. Dynamical Systems VI*, volume 6 of *Encyclopedia of Mathematical Sciences*. Springer-Verlag, Berlin, 1993. Russian original published in 1988.

[13] Michèle Audin. Hamiltonian monodromy via Picard-Lefschetz theory. *Comm. Math. Phys.*, 229(3):459–89, Sept. 2002. doi: 10.1007/s00220-002-0694-3.

[14] L. Bates and M. Zou. Degeneration of Hamiltonian monodromy cycles. *Nonlinearity*, 6: 313–335, 1993.

[15] L. M. Bates. Monodromy in the champagne bottle. *Z. Angew. Math. Phys.*, 42:837–847, 1991.

[16] A. V Bolsinov and A. T Fomenko. *Integrable Hamiltonian systems : geometry, topology, classification*. Chapman & Hall/CRC, Boca Raton, Fla., 2004.

[17] Henk Broer, Konstantinos Efstathiou, and Olga Lukina. A geometric fractional monodromy theorem. *Discr. Cont. Dyn. Syst. – Ser. S*, 3(4):517–532, 2010. ISSN 1937-1632. doi: 10.3934/dcdss.2010.3.517.

[18] W. Burnside. *Theory of groups of finite order*. Cambridge Univ. Press, 2nd edition, 1911. reprinted, Dover, New York, 1955.

[19] C. Chevalley. Invariants of finite groups generated by reflections. *Amer. J. Math.*, 67: 778–782, 1955.

[20] R. Cushman and H. Knörrer. The energy momentum mapping of the Lagrange top. In Heinz-Dietrich Doebner and Jörg-Dieter Hennig, editors, *Differential Geometric Methods in Mathematical Physics: Proceedings of an International Conference Held at the Technical University of Clausthal, FRG, August 30–September 2, 1983*, pages 12–24. Springer Berlin Heidelberg, Berlin, Heidelberg, 1985. ISBN 978-3-540-39585-0. doi: 10.1007/BFb0074575.

[21] R. H. Cushman and L. Bates. *Global aspects of classical integrable systems*. Birkhäuser, Basel, 1997.

[22] R. H. Cushman and F. Beukers. The complex geometry of the spherical pendulum. *Celest. Mech. Contemp. Math.*, 292:47–70, 2002. see http://www.math.uu.nl/people/beukers/cspend.pdf for an extended and corrected version.

[23] R. H. Cushman and J. J. Duistermaat. The quantum-mechanical spherical pendulum. *Bull. Am. Math. Soc.*, 19:475–479, 1988.

[24] R. H. Cushman and J. J. Duistermaat. Non-Hamiltonian monodromy. *J. Diff. Eqs.*, 172: 42–58, 2001.

[25] R. H. Cushman and D. A. Sadovskiĭ. Monodromy in perturbed Kepler systems: hydrogen atom in crossed fields. *Europhys. Lett.*, 47:1–7, Jul 1999.

[26] R. H. Cushman and D. A. Sadovskiĭ. Monodromy in the hydrogen atom in crossed fields. *Physica D*, 142:166–96, Aug 2000.

[27] R. H. Cushman and San Vũ Ngọc. Sign of the monodromy for Liouville integrable systems. *Ann. H. Poincaré*, 3:883–894, 2002.

[28] Richard H. Cushman. Geometry of the energy-momentum mapping of the spherical pendulum. *Centrum voor Wiskunde en Informatica Newsletter*, 1:4–18, 1983.

[29] Richard H. Cushman and L. Bates. Complete integrability beyond Liouville–Arnold. *Rep. Mth. Phys.*, 56(1):77–91, 2005.

[30] Richard H. Cushman and L. Bates. Scattering monodromy and the A_1 singularity. *CEJM*, 5(3):429–451, 2007.

[31] J. B. Delos, G. Dhont, D. A. Sadovskiĭ, and B. I. Zhilinskiĭ. Dynamical manifestations of Hamiltonian monodromy. *Ann. Phys.*, 324:1953–1982, Sep 2009. ISSN 0003-4916. doi: 10.1016/j.aop.2009.03.008.

[32] John B. Delos, Guillaume Dhont, D. A. Sadovskiĭ, and B. I. Zhilinskiĭ. Dynamical manifestations of Hamiltonian monodromy. *Europhys. Lett.*, 83:24003/1–6, Jul 2008. doi: 10/1209/0295-5075/83/24003.

[33] J. J. Duistermaat. On global action-angle coordinates. *Comm. Pure Appl. Math.*, 33:687–706, 1980.

[34] Holger R. Dullin and Holger Waalkens. Nonuniqueness of the phase shift in central scattering due to monodromy. *Phys. Rev. Lett.*, 101:070405/1–4, Aug 2008. doi: 10.1103/PhysRevLett.101.070405.

[35] K. Efstathiou and H. W. Broer. Uncovering fractional monodromy. *Commun. Math. Phys.*, 324(2):549–588, 2013. ISSN 1432-0916. doi: 10.1007/s00220-013-1816-9.

[36] K. Efstathiou and D. A. Sadovskiĭ. No polar coordinates. lectures by Richard Cushman. In James Montaldi and Tudor Ratiu, editors, *Geometric Mechanics and Symmetry. The Peyresq Lectures*, London Mathematical Society Lecture Note Series No. 306, pages 211–302. Cambridge University Press, 2005.

[37] K. Efstathiou and D. A. Sadovskiĭ. Normalization and global analysis of perturbations of the hydrogen atom. *Rev. Mod. Phys.*, 82(3):2099–2154, Aug 2010. doi: 10.1103/RevModPhys.82.2099.

[38] K. Efstathiou, D. A. Sadovskiĭ, and B. I. Zhilinskiĭ. Classification of perturbations of the hydrogen atom by small static electric and magnetic fields. *Proc. Roy. Soc. London, Ser. A*, 463:1771–1790, Jul 2007. doi: 10.1098/rspa.2007.1843.

[39] K. Efstathiou, O. V. Lukina, and D. A. Sadovskiĭ. Complete classification of qualitatively different perturbations of the hydrogen atom in weak near orthogonal electric and magnetic fields. *J. Phys. A: Math. Theor.*, 42:055209/1–29, 2009. doi: 10.1088/1751-8113/42/5/055209.

[40] K. Efstathiou, A. Giacobbe, P. Mardešić, and D. Sugny. Rotation forms and local Hamiltonian monodromy. arXiv:1608.01579 [math-ph], August 4 2016.

[41] H. Flaschka. A remark on integrable Hamiltonian systems. *Phys. Lett. A*, 131(9):505–508, 1988.

[42] L. Gavrilov and O. Vivolo. The real period function of the A_3 singularity and perturbations of the spherical pendulum. *Comp. Math.*, 123:167–184, 2000.

[43] Lubomir Gavrilov and Iliya D Iliev. The displacement map associated to polynomial unfoldings of planar Hamiltonian vector fields. *Am. J. Math.*, 127(6):1153–1190, 2005.

[44] Gert-Martin Greuel, Christoph Lossen, and Eugenii Shustin. *Introduction to Singularities and Deformations*. Springer Monographs in Mathematics. Springer-Verlag, Berlin–Heidelberg, 2007.

[45] Valentine S. Kulikov. *Mixed Hodge Structures and Singularities*, volume 132 of *Cambridge Tracts in Mathematics*. Cambridge University Press, 1998. ISBN 9780521620604.

[46] L. Michel and B. I. Zhilinskiĭ. Symmetry, invariants, topology. Basic tools. *Phys. Rep.*, 341:11–84, 2001.

[47] Henri Mineur. Etude des systèmes admettant *n* intégrales premières uniformes en involution. extension à ces systèmes des conditions de quantification de Bohr–Sommerfeld. *J. Ecole Polytech., Sér. III*, 143:237–270, 1937.

[48] N. N. Nekhoroshev, D. A. Sadovskiĭ, and B. I. Zhilinskiĭ. Fractional monodromy of resonant classical and quantum oscillators. *Comptes Rendus Acad. Sci. Paris, Sér. I*, 335:985–8, Dec 2002.

[49] N. N. Nekhoroshev, D. A. Sadovskiĭ, and B. I. Zhilinskiĭ. Fractional Hamiltonian monodromy. *Ann. H. Poincaré*, 7:1099–211, 2006. doi: 10.1007/s00023-006-0278-4.

[50] Nikolaĭ N. Nekhoroshev. Two theorems on the action-angle variables. *Uspekhi Mat. Nauk*, 24(5):2, 1969. in Russian.

[51] Nikolaĭ N. Nekhoroshev. Angle-action variables and their generalizations. *Trans. Moscow Math. Soc.*, 26:180–198, 1972.

[52] Nikolaĭ N. Nekhoroshev. Theorem of Poincaré-Lyapunov-Liouville-Arnol'd. *Funk. Analiz*, 28(2):3, 1994.

[53] Nikolaĭ N. Nekhoroshev. Fractional monodromy in the case of arbitrary resonances. *Sbornik Math.*, 198:383–424, 2007. doi: 10.1070/SM2007v198n03ABEH003841.

[54] Nikolaĭ N. Nekhoroshev. Fuzzy fractional monodromy and the section–hyperboloid. *Milano J. Math.*, 76:1–14, 2008. doi: doi:10.1007/s00032-008-0085-0. Presented at the Seminario Matematico e Fisico di Milano, November 8, 2004.

[55] Nikolaĭ N. Nekhoroshev. Monodromy of the fibre with oscillatory singular point of type $1{:}(-2)$. *Russ. J. Nonlin. Dyn.*, 12(3):413–541, 2016. doi: 10.20537/nd1603008. in Russian, manuscript dated April 2008.

[56] Zung Nguyên Tiên. A note on focus-focus singularities. *Diff. Geom. and Appl.*, 7:123–130, 1997. doi: 10.1016/S0926-2245(96)00042-3.

[57] Zung Nguyên Tiên. Another note on focus-focus singularities. *Lett. Math. Phys.*, 60:87–99, 2002.

[58] J. P. Ortega and T. S. Ratiu. Singular reduction of Poisson manifolds. *Lett. Math. Phys.*, 46:359–372, 1998.

[59] D. A. Sadovskiĭ and B. I. Zhilinskiĭ. Monodromy, diabolic points, and angular momentum coupling. *Phys. Lett. A*, 256:235–44, Jun 1999. doi: 10.1016/S0375-9601(99)00229-7.

[60] D. A. Sadovskiĭ and B. I. Zhilinskiĭ. Quantum monodromy and its generalizations and molecular manifestations. *Mol. Phys.*, 104:2595–615, Aug 2006. doi: 10.1080/00268970600673363.

[61] Dmitriĭ A. Sadovskiĭ. Classical and quantum Hamiltonian monodromy: a case study of the hyperbolic circular billiard. This manuscript, intended as a popular chapter for physicists, was largely written in 2008, Jul 2010.

[62] Richard P. Stanley. Invariants of finite groups and their applications to combinatorics. *Bull. Amer. Math. Soc.*, 1(3):475–511, 1979.

[63] B. Sturmfels. *Algorithms in invariant theory*. Springer Verlag, Berlin, 1993.

[64] D. Sugny, P. Mardešić, M. Pelletier, A. Jebrane, and H. R. Jauslin. Fractional Hamiltonian monodromy from a Gauss-Manin monodromy. *J. Math. Phys.*, 49:042701–35, Apr 2008. doi: 10.1063/1.2863614.

[65] Margaret Symington. Four dimensions from two in symplectic topology. In G. Matic and C. McCrory, editors, *Topology and geometry of manifolds*, volume 71 of *Proc. Sympos. Pure Math.*, pages 153–208. Amer. Math. Soc., Providence, Rhode Island, 2003.

[66] D. I. Tonkonog. A simple proof of the geometric fractional monodromy theorem. *Mosc. Univ. Math. Bull.*, 68(2):118–121, 2013. ISSN 1934-8444. doi: 10.3103/S0027132213020095.

[67] Olivier Vivolo. The monodromy of the Lagrange top and the Picard-Lefschetz formula. *J. Geom. Phys.*, 46:99–124, 2003.

[68] San Vũ Ngọc. Quantum monodromy in integrable systems. *Commun. Math. Phys.*, 203: 465–79, 1999.

[69] San Vũ Ngọc. Bohr–Sommerfeld conditions for integrable systems with critical manifolds of focus-focus type. *Commun. Pure & Appl. Math.*, 53:143–217, 2000.

[70] San Vũ Ngọc. Moment polytopes for symplectic manifolds with monodromy. *Adv. Math.*, 208:909–934, 2007.

[71] H. Waalkens. Quantum monodromy in trapped Bose condensates. *Europhys. Lett.*, 58: 162–168, 2002.

[72] H. Weyl. *Classical groups. Their invariants and representations*. Princeton University Press, New Jersey, 1939.

[73] M. Winnewisser, B. P. Winnewisser, I. R. Medvedev, F. C. De Lucia, S. C. Ross, and L. M. Bates. The hidden kernel of molecular quasi-linearity: Quantum monodromy. *J. Mol. Struct.*, 798:1–26, 2006. doi: 10.1016/j.molstruc.2006.06.036|ISSN0022-2860.

[74] Boris I. Zhilinskiĭ. Interpretation of quantum Hamiltonian monodromy in terms of lattice defects. *Acta Appl. Math.*, 87(1):281–307, May 2005. doi: 10.1007/s10440-005-1164-7.